DEVELOPMENT OF AN ION-SCATTERING SYSTEM

Development of a Low-Energy Ion Scattering Surface Analysis System Using a Time-of-Flight Method

by

Andrew Claude Cervin, B.Sc.

A Project
Submitted to the School of Graduate Studies
in Partial Fulfillment of the Requirements
of the Degree
Master of Engineering

McMaster University
1981

MASTER OF ENGINEERING
(Engineering Physics)

McMASTER UNIVERSITY
Hamilton, Ontario

TITLE: Development of a Low-Energy Ion Scattering System using a Time-of-Flight Method

AUTHOR: Andrew Claude Cervin, B.Sc. (University of Windsor)

SUPERVISOR: Dr. Philip Lichtenberger

NUMBER OF PAGES: vi, 62

ABSTRACT

An ion scattering surface analysis system using TOF energy-analysis of the scattered ions was improved with a duoplasmatron ion source and new data-handling electronics. The new source gave greater beam current and stability. The new electronics were: a timing filter amplifier and constant fraction discriminator.

Much work was done on alignment of the sample in the beam and reduction of the spot size. To add to the flexibility of the beam guidance system a new pair of steering plates was added.

Some of the test spectra are presented to show the operation of the system. Relevant material on various aspects of the system are presented in the appendices.

ACKNOWLEDGEMENTS

I am very grateful to Dr. Phil Lichtenberger for his help and guidance throughout this project. I also thank Peter Ganza for much work on the power supply and beam steering electronics.

The work was done under an NSERC postgraduate scholarship. I thank NSERC for the scholarship and the fine service they provided.

I would like to thank Janet Arsenault for typing this report, and my parents for much help and support.

TABLE OF CONTENTS

		Page
CHAPTER 1:	INTRODUCTION	1
CHAPTER 2:	SINGLE COLLISION MODEL	2
	2.1 Introduction	2
	2.2 Asymptotic Values of E and P	2
	2.3 Justification of Single-Collision Model	4
	2.4 Damage Caused by Ion Impact	6
	2.5 LEIS as a Surface Analysis Technique	8
CHAPTER 3:	ION SCATTERING TECHNIQUES	10
	3.1 Introduction to Surface Analysis with LEIS	10
	3.2 Surface Analysis with ESA	11
	3.3 Surface Analysis with TOF	12
	3.4 Comparison of TOF and ESA Surface Analysis	14
CHAPTER 4:	EXPERIMENTAL SYSTEM DEVELOPMENT	15
	4.1 Current Configurations System	15
	4.2 Development of the System	17
	4.3 Problems Encountered During System Development	19
	4.4 Further Possible Improvements	20
CHAPTER 5:	RESULTS	22
CHAPTER 6:	SUMMARY	24
FIGURES		25
APPENDICES:	A. Ion Beams and Lenses	36
	B. Vacuum Devices and Concepts	42
	C. Duoplasmatron Ion Source	56
REFERENCES		62

LIST OF ILLUSTRATIONS

		Page
Fig. 4.1:	Top View of Vacuum System	25
Fig. 4.2:	Faraday Cup Assembly	26
Fig. 4.3:	Circuit Diagram for Beam Chopping Pulser	27
Fig. 4.4:	Block Diagram of Deflection Plate Control	28
Fig. 4.5:	Carousel Assembly	29
Fig. 4.6:	Deflection Plate Assembly	30
Fig. 4.7:	Block Diagram of TOF Electronics	31
Fig. 5.1-5.4:	TOF Spectra	32-35
	Cutaway View of Oil Diffusion Pump	50
Fig. C-1	Cutaway View of Ion Source	59
Fig. C-2	Source Interconnection and Supplies	60
Fig. C-3	Circuit Diagram of Ion Source Power Supply	61

CHAPTER 1

INTRODUCTION

This report details the improvment of a low-energy ion-scattering (LEIS) surface-analysis system. Development concentrated mainly on the ion source and sample manipulation/alignment.

Chapter 1 gives an introduction to the basic ideas of ion scattering, and justification of assumptions made in the development of the equations.

Chapter 2 compares the two major LEIS methods of surface analysis. Reasons for using the TOF method are given.

Chapter 3 describes the final configuration of the system reached after the work on the ion source and sample alignment was finished. The development process and further improvements that could make the system more versatile and useful, are described.

Chapter 4 presents details of some test results obtained during development.

The appendices contain relevant details and theory of electrostatics (lenses, energy analyzers, etc.), vacuum devices, and the duplasmatron ion source.

CHAPTER 2

SINGLE COLLISION MODEL

2.1 Introduction

Scattering of atomic particles is the deflection of each particle from its free-flight path by another particle, usually by an electrostatic interaction. Neutron scattering is different as there is no electrostatic interaction but only hard-sphere scattering, primarily with nuclei of target atoms.

The details of an electrostatic interaction between an ion projectile and a neutral target atom are complicated, involving screened Coulomb potentials. The Thomas-Fermi potential gives greatest accuracy but is the most involved. At the low energies used in this experiment the screening terms take on significant values because the distance of closest approach is large. Large screening terms lead to complexity of calculation. The unscreaned Coulomb potential is used here to outline the concepts applicable to the process of ion scattering and not to provide a basis for accurate calculation.

Asymptotic values of the energy and momentum after the scattering event are easy to calculate and provide the basis for discussion of the energy spectrum of the scattered particles.

2.2 Asymptotic Values of E and P

Details of the scattering interaction are neglected here and a

simple, classical analysis of the scattering geometry is presented.

The scattering event involves two particles: the projectile ion and the target atom, initially at rest. The projectile ion has velocity v_1 and energy E_o:

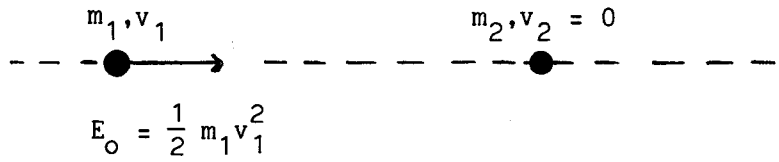

After the interaction we have:

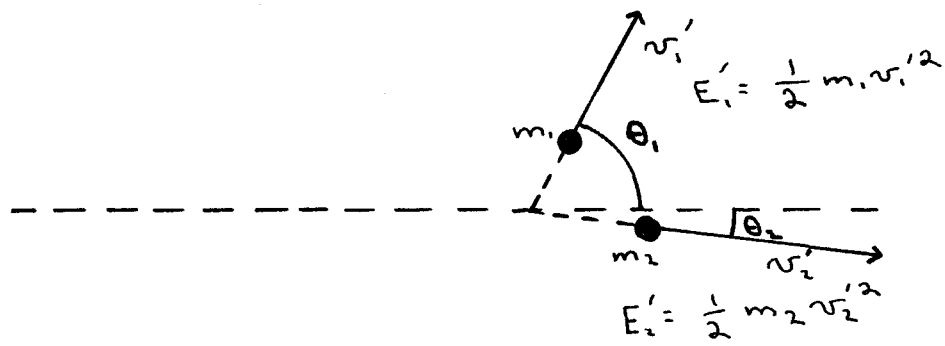

Figure 2.1

Manipulation of the energy and momentum conservation equations yields[1]:

$$\frac{E_1'}{E_o} = \frac{m_1^2}{(m_1+m_2)^2} \{[\cos\theta_1 + ((\frac{m_2}{m_1})^2 - \sin^2\theta_1)^{1/2}]^2\}$$

This equation determines the character of the experiment: θ_1 is fixed and then the energy of the scattered particles is measured to obtain an energy spectrum. From the structure of the spectrum the masses of the target particles may be determined: each target particle of a certain m_2 scatters particles into a fixed angle with a certain E_1'.

If more than simple identification of target atoms is required, i.e., if stochiometric ratios must be found, then the details of interaction must be followed through. Calculating ratios of elements requires the cross-section for scattering, and calculation of that requires the use of screened Coulomb potentials.

The Rutherford scattering cross-section is presented here to give an idea of how penetration depths, reflection coefficients, etc. vary with mass of target and projectile particles, and incident energy. The Rutherford cross-section assumes an unscreened Coulomb potential[1]:

$$d\omega \{\sigma(E_1\theta_1) = \frac{1}{16} \frac{(Z^2_1 Z^2_2 e^4)}{E^2 \sin^4(\frac{\theta_1}{2})} d\omega$$

e = unit charge

Z_1 = charge number of incident ion nucleus

Z_2 = charge number of target nucleus

and

$\sigma(E,\theta_1)d\omega$ = probability of a particle of energy E_o being scattered into solid angle $d\omega$, at angle θ_1

Thus, cross-section decreases with increasing energy or angles, and increasess with increasing charge of either target or projectile particle.

2.3 Justification of Single-Collisional Model

The single collision model makes a few assumptions as to the conditions of the experiment: non-relativistic particles, single collision, small penetration depths (a few atomic layers), and immobile

target atoms.

The energies used in the experiment were between three and ten Kilovolts (KeV). The lightest projectiles used were protons. For protons at 10 KeV, $\frac{v}{c} \simeq 6 \times 10^{-3}$, well below any relativistic effects. The target atoms were at room temperature. Therefore they had thermal energy of around .03 eV. Compared with the incident energy of a few KeV this is negligible and thus the target particles could be assumed to be at rest for the duration of the collision.

There are two types of energy loss for an ion in a solid: electronic, and nuclear.

Electronic energy loss is given by[4]:

$$\left(\frac{dE}{dx}\right)_e = - KE^{1/2}$$

$$K = Z_1^{1/6} \left\{\frac{Z_1 Z_2 8\pi e^2 a_o N}{(Z_1^{2/3}+Z_2^{2/3})^{3/2} \sqrt{E'}}\right\}$$

a_o = Bohr radius

E' = energy where ion velocity equals velocity of electron in first Bohr orbit (E' = 25 KeV for H)

N = atomic density.

Thus electronic energy loss is proportional to velocity. For 10 KeV H^+ in Au; $\left(\frac{dE}{dx}\right)_e = -6.84 \times 10^{-3}$ kev/A. Therefore electronic stopping is negligible at these energies. Thus most of the energy loss occurs from collisions with target nuclei. When electron energy loss is negligible ($K \backsim 0$) as is the case here, the probability of a scattering event in path length dx is[4]:

$$dP = N\,\sigma\,(E_1,\theta_1)\,d\omega dx$$

$\therefore$ $P(x_o)$ = probability that scattering event takes place at depth x_o into surface

$$= \int_o^{x_o} N\,\sigma\,(E_1\theta_1)\,d\omega dx = (N\,\sigma\,(E_1\theta_1)d\omega)\,x_o$$

Thus maximum depth of penetration ($P(x_o) = 1$) is given by:

$$x_o = \frac{1}{N\sigma(E_1\theta_1)d\omega}$$

For Rutherford cross-section:

$$x_o = \frac{16\,E_1^2\,\sin^4(\theta/2)}{N\,Z_1^2\,Z_2^2\,e^4\,dw}$$ = maximum depth of penetration for particles scattered into $d\omega$ at θ.

Therefore penetration increases with increasing energy and scattering angle and decreases with increasing z. x_o was obtained assuming a single collision but obviously the probability of multiple collisions increases with path length inside the target. The assumption of single collisions is justified for low energies, heavy target and projectile particles, but for higher energies and lighter particles (less charge in nucleus) the possibility of multiple collisions is greatly increased and does appear in the energy spectrum of the scattered particles.

2.4 Damage Caused by Ion Impact

In a scattering event energy is transferred to the target atom. Transferred energy must be absorbed by the crystal and thus produces disorder, heating of the target, dislocations, etc. A qualitative idea of the relative amounts of damage caused by projectiles on different

targets can be obtained by considering maximum transferred energy.

The energy transferred to a target atom is given by[4] (see Fig. 1.1):

$$E_2 = \frac{1}{2} m_2 v_2^2 = \frac{4 E_o m_1 m_2}{(m_1 + m_2)^2} \cos^2 \theta_2$$

Maximum energy transferred when $\theta_2 = 0$ is:

$\hat{E}_2$ = maximum transferred energy

$$= \frac{4 E_o m_1 m_2}{(m_1 + m_2)^2}$$

Values for two different projectiles incident on two different targets are presented below:

H^+ (m_1 =1)	He^+ (m_1 =4)	incident on
.133 E_o	.28 E_o	Si(m_2=28)
.02 E_o	.078 E_o	Au(m_2=197)

Fig. 2.2: $\hat{E}_2$ for different targets and projectile particles.

For E_o in the KeV range these transferred energies are greater than limiting energies of the lattice (< 10 eV). Therefore the primary knock-on (first target particle) will be ejected from its lattice position and produce cascades of damage until it comes to rest. The total amount of damage to the sample is proportional to the total dose received by the target (total number of particles incident on the target). Damage can be reduced by lowering incident energy, reducing

the dose, or using lighter projectile ions. Increasing target mass also reduces damage but is not always possible.

2.5 LEIS as a Surface Analysis Technique

Surface analysis is performed to acquire information primarily about the composition of a surface, i.e. the elements it consists of and their proportions. Of these two, the proportion of elements in the surface is not usually as important as the actual elements present. Thus, the two main parameters of interest when evaluating a surface analysis technique are: sensitivity to trace elements, and mass resolution.

Sensitivity to trace elements has been studied. It has been found that 10^{-3} monolayers is easily detectable once the surface has been cleaned properly. Identification of trace elements is straightforward because the energy of the peak is related to the mass of the target by Equation 1.

A decrease in resolution occurs because of surface sputtering and deeply penetrating ions. These create a low energy tail that continues down to very small energies, and may obscure peaks from light elements[1]. Reducing incident energy reduces sputtering and penetration depth, decreasing the low energy tail.

Ratios of elements are more difficult to obtain. The cross-section for the elements in question must be calculated with the proper potential, and background noise must be taken into account. Efforts in this direction have med with mixed results[1].

LEIS has higher surface sensitivity than the main competing technique, Auger Electron Spectroscopy (AES). The electrons used in AES penetrate deeply because of their small charge and high velocity. LEIS has an advantage as well in that elements are readily identified. Surface damage is higher than with AES, especially if heavier (e.g. Ar^+) ions are used.

CHAPTER 3

ION SCATTERING TECHNIQUES

3.1 Introduction to Surface Analysis with LEIS

As described in Section 1.2 the basic scattering experiment consists of fixing the scattering angle, bombarding the target with a suitable ion beam, and analysing the scattered energy. Differences between systems exist only in the method of analysing the energy of the scattered particles.

All surface analysis systems using LEIS have essentially the same configuration, for good reasons. An ultra-high vacuum chamber ($< 10^{-9}$ Torr), pumped by a non-contaminating pump, holds the target manipulator and energy analyser. An ion source provides a well-collimated ion beam of suitable energy and composition. These two sections are connected to each other through a differential pumping section which buffers the high gas load in the source section and maintains the ultra-high vacuum in the target section. The differential section usually has collimating apertures and deflection plates to guide the beam.

The two main types of energy analysis methods compared are: the electrostatic analyser (ESA) and time-of-flight (TOF) methods. The advantages and disadvantages of each technique will be discussed in the rest of this chapter.

3.2 Surface Analysis with ESA

The ESA consists of an electric sector field with entrance and exit slits (see Appendix A). A detector (usually a channel electron multiplier) senses the particles at the exit slit. The static electric field allows only particles with a certain energy through, determined by the voltage on the plates. Resolution depends on slit width and path length through the ESA.

Energy spectra are accumulated point by point over the range of interest.

Energy resolution of ESA systems are usually between 4% and 5%[1,2]. ESA's have around 3% energy resolution. Higher peak widths can be attributed to beam energy spread and detector solid angle subtended at the target as well as multiple scattering and sputtered particles. Resolution degradation by these factors is common to all ion scattering systems.

The ESA detects only ions. Neutralized particles are not analysed. Studies made on neutralization of reflected ions show that at low energies (2-5 KeV) between 80% and 90% of the scattered beam consists of neutrals. The ESA "discards" these particles and consequently, 80% of available data. Attempts to reionize scattered particles with a high pressure gas cell (10^{-6} torr) did not meet with much success.[3] The gas cell requires complicated differential pumping to avoid contamination of the target.

The TOF method solves these problems at expense of some resolution.

3.3 Surface Analysis with TOF

The time-of-flight technique for determining the energy of scattered particles measures the flight time of the particle between the scattering event and the detector. A long ($\sim$ 1 meter) flight tube is used to lengthen the flight time to a measurable quantity. Scattered particles are assumed to be in free flight between the target and detector. If the flight path length is known the conversion from the resulting time spectrum to an energy spectrum is easily done:

$$E_n = \frac{1}{2} m \frac{d^2}{t_n^2}$$

d = flight path length

t_n = time-of-flight for a particular channel

$$\Delta N_e = \frac{\Delta N_t}{\Delta E_i}$$

Δt_i = counts per energy interval

ΔN_t = counts per time interval

ΔE_i = i^{th} energy interval

Δt_i = i^{th} time interval

The detector is usually a channeltron but a Johnson mesh multiplier has been used in some systems[3]. These detectors are sensitive to neutral as well as charged particles. Thus all scattered particles (in the $d\omega$ subtended by the detector at the target) are detected.

To provide timing signals, the beam is electrically chopped with a pair of plates, usually in the differential section. The beam is held off the target by a voltage across the plates, then swept into the target by a voltage pulse added onto the D.C. voltage. The voltage

pulse also starts the timing circuits. Pulses from the detector stop the timing circuits, a time-to-pulse height converter (TPC). A pulse height analyser (PHA) provides a direct readout of the time spectrum. All energies are detected at once with no need to collect data at discrete points. The pulse starting the TPC can be delayed until the particles reach the target.

The charged fraction of the scattered particles can be measured with minor modification of the system. Charged particles entering the TOF leg can be deflected by a voltage across two plates and a spectrum of neutral particles can be accumulated. Subtracting this spectrum from a charged plus neutrals spectrum gives the charged fraction as a function of energy.

The minimum resolution obtainable with a TOF system is inherently worse than an equivalent ESA system. The reason for this is the detection of neutral particles. Particles that penetrate deeply into the surface undergo multiple collisions. These particles also have a higher probability of being neutralized. The ESA rejects all neutrals and thus the signal from deep within the surface. Thus the TOF resolution is limited by multiple collisions.

The experimental limits to resolution of a TOF system are set by a pulse width applied to the chopping plates. This is an uncertainty subject to system improvements, i.e., shorter plates would reduce ion flight-time thus allowing shorter pulses to be used (the ions take a certain time to pass between the plates and if the pulse is too short no ions will pass through). The ratio $\Delta t/t$ can be decreased by

lengthening the flight tube and thus increasing t. However, shortening the pulse and lenthening the flight tube reduce data collection rates.

Noise in TOF spectra occurs mainly from two sources: dark current of the channeltron, and neutrals in the incident beam. The channeltron noise is low-level and can be removed by a discriminator. Neutrals in the beam can be eliminated by misaligning the beam path and steering the beam into the apertures. The system described in this report has very low noise ($\sim$ -80db).

Channeltron efficiency must be taken into account when analysing the spectra. Efficiency at low energies (< 1 KeV) is small and so the spectra must be corrected. The spectra presented in Chapter 3 are uncorrected: however only the high energy side is shown, where efficiency is relatively uniform.

3.4 Comparison of TOF and ESA Surface Analysis

The main disadvantage of the ESA technique is that high doses are required (10^{15}) to obtain an acceptable numer of counts. The TOF method is a multiple-channel method (total spectrum gathered at once) and can analyse neutral particles. Charge fraction measurements can be done with minor modifications. Resolution, however, is generally poorer with TOF than with ESA[3] but with TOF it is possible to exchange data rates for resolution.

Target damage is one of the more important factors in surface analysis, thus TOF surface analysis is being used more frequently.

CHAPTER 4

EXPERIMENTAL SYSTEM DEVELOPMENT

4.1 Current Configuration of the System

Figure 4.1 shows a diagram of the current configuration of the system. The four main sections are shown.

The ion source was a Duaplasmatron Ion Source from Physicon Corporation. The power supply for it was built in-house. Appendix C has schematic and circuit diagrams of the source and power supply. An Einzel lens focussed the beam onto the first aperture, and deflecttion plates steered the beam into the mass analysing section. This section was pumped by an oil diffusion-rotary pump combination with a cold trap.

The mass analysing section consisted of a small magnet (1 KG max) that deflected the beam through a 20° vertical angle, permitting only one mass through. A second set of deflection plates steered the beam through an aperture to the differential pumping section.

The differential pumping section was approximately 6" in diameter and pumped by a 6 section ion pump and a titanium sublimation pump. The chopping and deflection plates were in the exit tube of this section. Two high vacuum straight-through valves allowed each of the three sections to be isolated.

The beam was steered into the final collimating aperture by the last set of deflection plates in the entrance tube to the UHV chamber. The last aperture had a Faraday cup on the back that could be opened and

closed to either allow the beam to pass or monitor the current (Fig. 4.2). The carousel in the centre of the chamber was fitted on the end of a rod which was mounted on a bellows rotary feed-through combination that allowed movement in all directions. Alignment with the beam was done with a grounded aperture close to a blank face on the carousel (Fig. 4.5). Current on the carousel was monitored and alignment was achieved by maximizing the current. Targets were glued to the carousel with silver paint.

The UHV chamber was pumped by a turbomolecular pump and a titanium sublimation pump (see Appendix B). These used no oil and consequently a clean vacuum resulted.

The flight tube could be mounted for scattering angles of 135° or 90°. A channeltron at the end was used to detect the scattered particles. The flight tube was 129.2 cm long and provided with plates at the entrance to allow charge fraction measurements to be made.

The electronics were standard nuclear instrumentation units. A channeltron preamplifier fed the pulses into an Ortec timing filter amplifier. An Ortec constant fraction discriminator provided the "stop" pulses. Timing was done with an Ortec time-to-amplitude convertor and the output pulses were analysed by a Tracor-Northern pulse-height analyser. A pulser providing 120V, 50 nsec pulses was used to chop the beam (Fig. 3.3). A delay line amplifier provided the "start" pulses to the TPC from the pulser. A block diagram of the electronics appears in Fig. 4.7.

Deflection plates were controlled by a specially-built panel (Fig.

4.4): ± 250 V were available for each plate. Beam current was monitored with a Keithley picoammeter.

Two other sample characterization systems were provided for in the basic design. A LEED-Auger unit (Low Energy Electron Diffraction) and Secondary ion Mass Spectrometer (SIMS) could be used with the UHV chamber. The LEED-Auger unit was not used. But the SIMS unit was used to do residual gas analysis to check the quality of the vacuum.

4.2 Development of the System

The initially available system consisted of the UHV, and differential sections, vacuum pump, TOF electronics flight tube, and SIMS unit with associated electronics.

Development was done in four areas: TOF electronics, duoplasmatron ion source, beam handling, and sample manipulation.

The, source and development of the power supply are described in Appendix C.

Sample manipulation originally consisted of: a goniometer holding one sample and allowing rotation in the horizontal and parallel to sample surface planes, and the carousel arrangement.

The goniometer centered the target in the chamber and allowed it to be pushed forward with a linear-motion feed through for analysis of sputtered products by the SIMS. The first change was a longer rod enabling the sample to be pushed further in order to reach the LEED-Auger unit. It was later found that the chamber was too small to allow satisfactory LEED photographs to be taken. This led to the

abandonment of the goniometer arrangement in favour of the carousel arrangement (Fig. 4.5). A phosphor (MgO_2) mounted on the carousel helped to align the beam.

The TOF electronics originally consisted of: channeltron and preamplifier, linear amplifier, cross-over pickoff, time-to-amplitude (TAC) confertor, and a PHA. The pulser, delay line amplifier, and TAC remain. The linear-amplifier cross-over pick-off combination gave very poor spectra. Observation of channeltron pulses on an oscilloscope showed that the cross-over varied somewhat and an uncertainty of $\sim \pm 1$ μsec occurred. This was more than enough to destroy resolution. The linear amplifier-cross-over pick-off pair were replaced by a timing filter amplifier-constant fraction discriminator pair. This gave possible resolution to tens of nanoseconds. The spectra improved but resolution was still below what was expected from the pulse width and flight tube length.

Beam steering was done with deflection plates (Fig. 4.6). Four pairs of plates were used in front of each aperture (see Fig. 4.1). The Faraday cup (Fig. 4.2) had two apertures selected by moving the assembly up and down with a linear feedthrough. A large aperture for sputter cleaning and a small aperture for TOF analysis were used. In an effort to obtain better resolution the small aperture was reduced from 1.5 to .7 mm. This improved resolution a little but reduced beam current as well. Reduced spot size was around 2 mm in diameter (estimated from phosphor).

4.3 Problems Encountered during System Development

Two areas gave problems throughout the course of development: ion beam stability and current, and resolution. The ion beam problems were overcome but poor resolution remains a problem.

The ion beam source gave 2-300 nanoamps of current (H^+) on target at 5 KeV. Spot size was about 2 mm in diameter. This amount of current gave acceptable count rates for Au targets but for silicon targets the count rate was just barely usable.

A problem occurred at high energies with the gas feed line. It was necessarily plastic because the source floated at the accelerating potential. Above 8 KeV, arcing occurred through the tube and shut down the source. Lengthening the tube reduced the arcing until accelerating voltage reached 9.5 KeV, which was acceptable.

After running the source all day for a few days the performance deteriorated drastically. The deterioration was found to be caused by oxide buildup in the arc area. Cleaning was required after long runs.

The first power supply for the arc used a silicon-controlled-rectifier (SCR) as a switch to provide the voltage pulse for starting the arc. The transients produced when starting, eventually blew out the SCR. The final power supply eliminated the problem, by using a high-power transistor to control the current.

Poor resolution remained a problem during the whole development process. Spot size was reduced, flight tube lengthened, and electronics changed. None of these gave any substantial decrease in peak width. The beam energy spread was equivalent to $\sim$ .06 μsec, much less than

observed resolution. Eventually the channeltron was examined and found to be fractured. This could have caused a deterioration in pulse shape and consequent mistracking of the constant fraction discriminator. It could not be tested, but replacement of the channeltron should improve the resolution by giving a consistent pulse shape. This was partially confirmed by the much better resolution of the He+ spectra (Fig. 4.4). The heavier He+ ions may have produced more primary electrons and thus a better pulse shape.

4.4 Further Possible Improvements

The main areas where improvement is needed immediately are: resolution and ultimate vacuum. Other improvements, now so urgent, would make the system more versatile and useful.

Resolution could probably be improved by installation of a new channeltron. Then other factors would limit the resolution, such as: pulse width, beam energy spread, etc. A more efficient detector such as a Johnson mesh multiplier could be installed to increase count rate.

The ultimate pressure could be lowered by a more efficient baking system. The pumps are quite capable of 10^{-10} torr but the system needs to be cleaned and baked properly.

A new sample manipulator is not so urgent but would make the system more useful. Sample cleaning and heating should make it possible to get a clean, well-ordered surface for analysis. The original goniometer arrangement would allow surface cleaning devices such as a sputter gun and a sample heater to be used and a single sample could then be

thoroughly characterized, and possibly depth profiled as well, with the sputter gun.

Major modifications to the basic configuration are needed to accomodate the LEED-Auger unit. The UHV chamber is too small to allow its use. The TOF system should be developed first however, before these modifications are attempted.

CHAPTER 5

RESULTS

The four spectra presented here contain test results obtained during development of the system.

The first spectrum (Fig. 5.1) was obtained with 6 KeV H^+ scattered off a silicon surface at a scattering angle of 135^o. The silicon surface was a (111) plane and uncleaned. The 4 channel leading edge of the peak was obtained with very careful positioning of the sample in the beam. Time per channel was 62.4 nsec. Thus 4 channels in the leading edge translates into .25 μsec. H^+ scattered from Si at 135^o has energy $E_1' = .8833\ E_o$ (Eq. (1)). For E_o = 6 KeV the difference between the 6 KV channel and the silicon peak channel is 0.77 μsec. Resolution is obviously very poor. Absorbed gases cannot account for the shift in the peak. The absorbed gas would be mainly oxygen which would have shifted the peak .14 μsec, not enough to explain the width.

Figure 5.2 shows the result of scattering 5 KeV H^+ off Si at 90^o. The angle of incidence was 45^o. Both reducing the energy and reducing the angle result in a larger cross section and in consequence the second spectrum is narrower and has a narrower leading edge (.19 μsec). This could be explained by the presence of oxygen in the surface. The reduction in the low energy tail compared to the 6 KeV spectrum suggests that it is caused by sputtered particles and multiple collisions.

Figure 5.3 shows the spectrum of 6 KV H^+ scattered off Au at 135^o.

The leading edge is well-defined and narrow and there is very little tail. Au atoms are much heavier and have larger Z than Si, consequently nuclear cross-section is much higher, and sputtering is lower because of the lower transferred energy. These factors reduce the tail considerably, as is demonstrated. The number of backscattered particles is much greater than Si, 12000 counts in the peak, again because of the increased cross section.

The fourth spectrum (Fig. 5.4) was taken with He^+ as the projectile and Au as the target. A peak width of 2 channels was obtained here, close to the expected resolution of the system. Whatever mechanism caused the poor resolution with H^+ projectiles did not operate with the heavier ions. Some narrowing of the peak was expected because of the change in cross-section between H^+ and He^+, but it should have been less than that obtained when going from Si to Au. Possibly the channeltron works better with heavier particles.

The long low-energy tail was caused by sputtered particles. With a heavy ion, transferred energy is greater, thus more sputtering occurs.

The low number of counts was caused by the beam stability; the He^+ beam only operated for about 10 minutes. Pulse width had to be increased to allow the slow He^+ ions to traverse the chopping plates before the pulse ended. Pulse width was about 60 nsec.

CHAPTER 6

SUMMARY

The change from cold cathode discharge ion source to duo-plasmatron ion source resulted in an increase in current available on the target. The source produced a well-defined (2 mm spot size), monoenergetic beam with few neutrals. As a result the count rate were increased considerably.

Sample alignment was a critical factor. With the small sample area available on the carousel face a slight misalignment destroyed the spectrum completely. The best methods of alignment are those that allow the beam to be observed on the carousel.

Resolution with H^+ improved slightly over previous results with the initial system[4], and greatly when heavier (He^+) ions were used to bombard the target. Efforts were made to further improve resolution. Eventually, all other possibilities having been exhausted, the channeltron was examined and a fracture was found in the tube. The fracture could have caused some variation in the pulse shape with H^+ producing mistracking off the constant fraction discriminator. However the more massive He^+ ions produced more initial electrons and thus a more consistent pulse shape. A new channeltron, which was not available at the time, should produce better spectra.

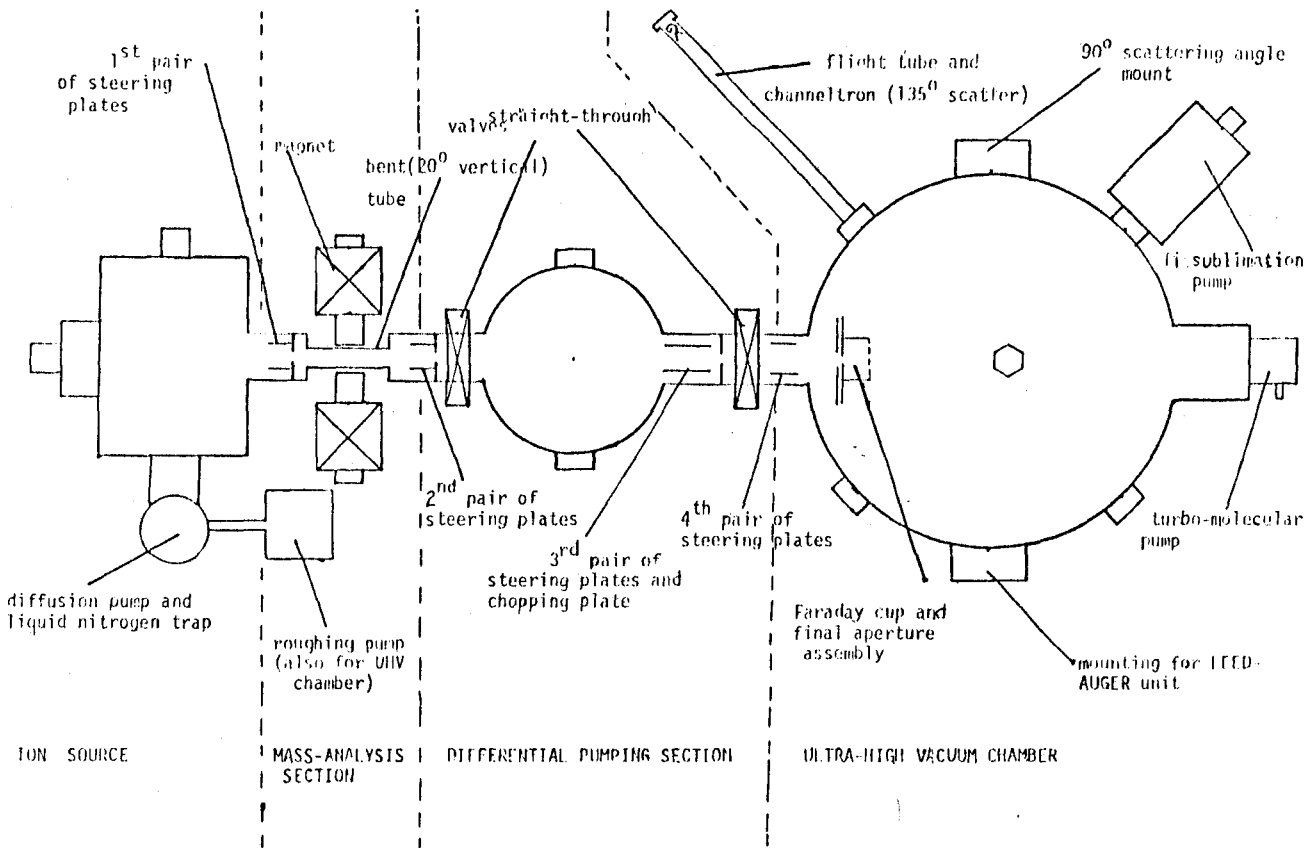

4.1 Top View of Vacuum System

4.2 FARADAY CUP ASSEMBLY

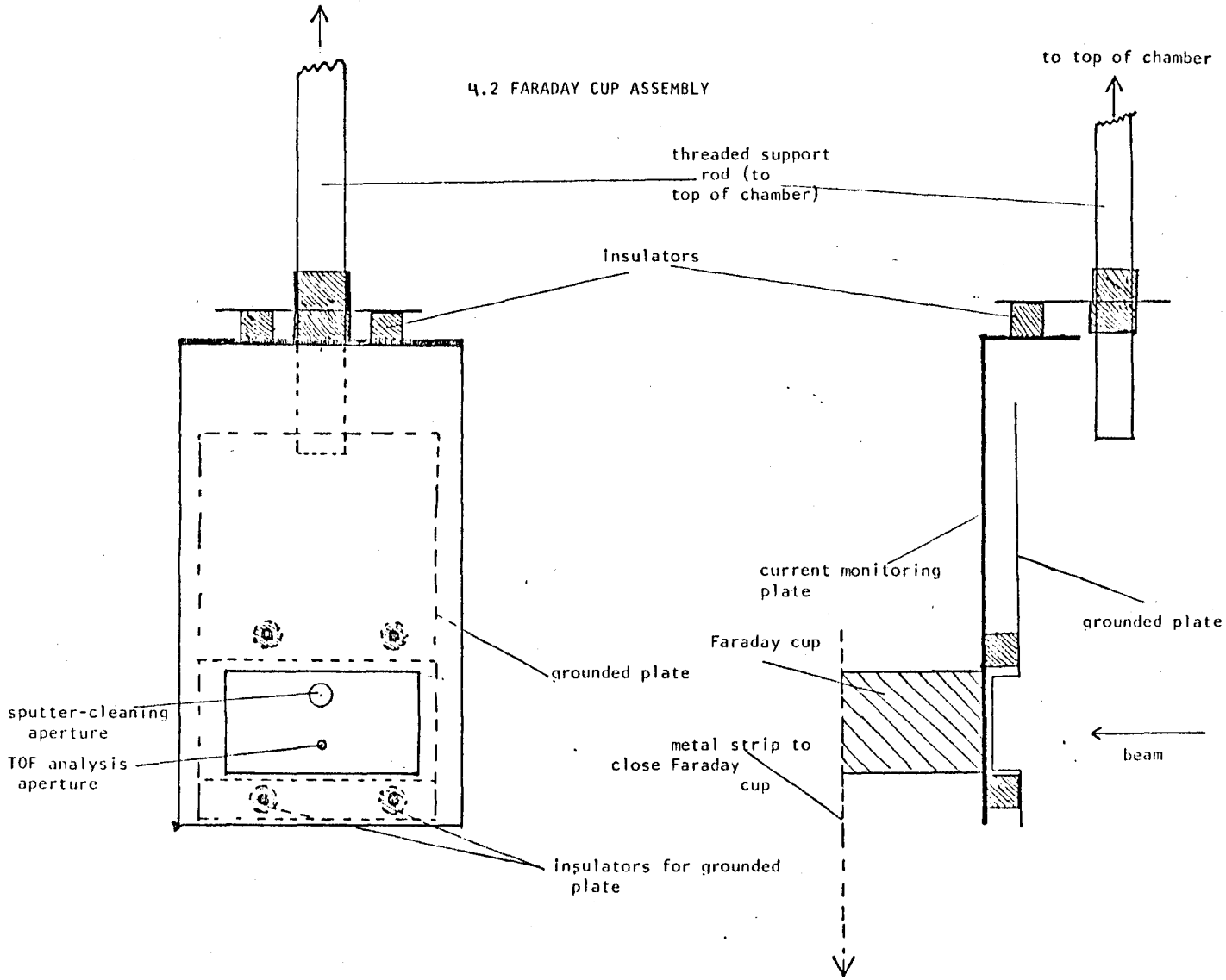

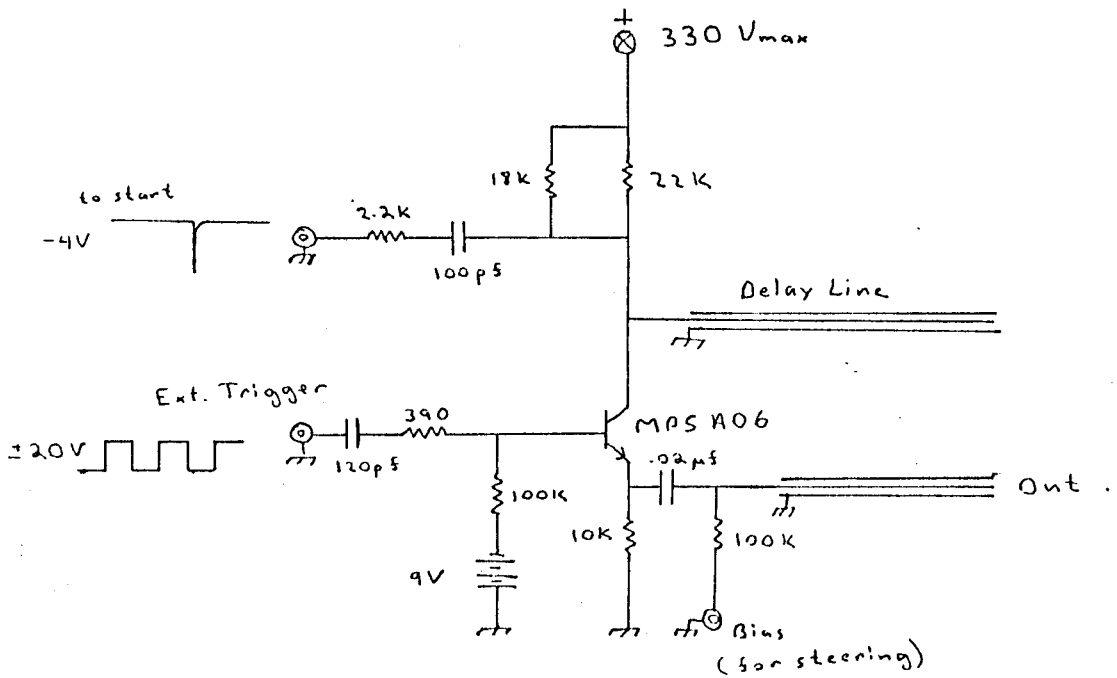

pulse: +120 volts
50 nsec long
3 nsec risetime

4.3 CIRCUIT DIAGRAM FOR BEAM CHOPPING PULSER

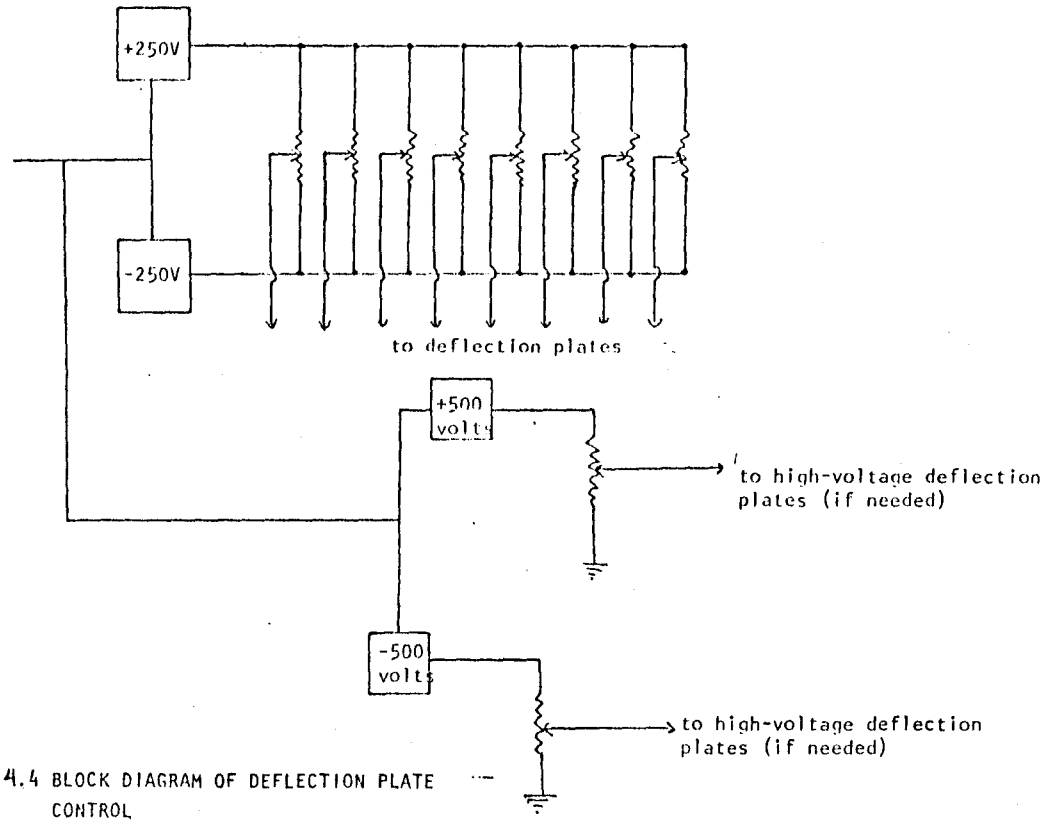

4.4 BLOCK DIAGRAM OF DEFLECTION PLATE CONTROL

4.5 CAROUSEL ASSEMBLY

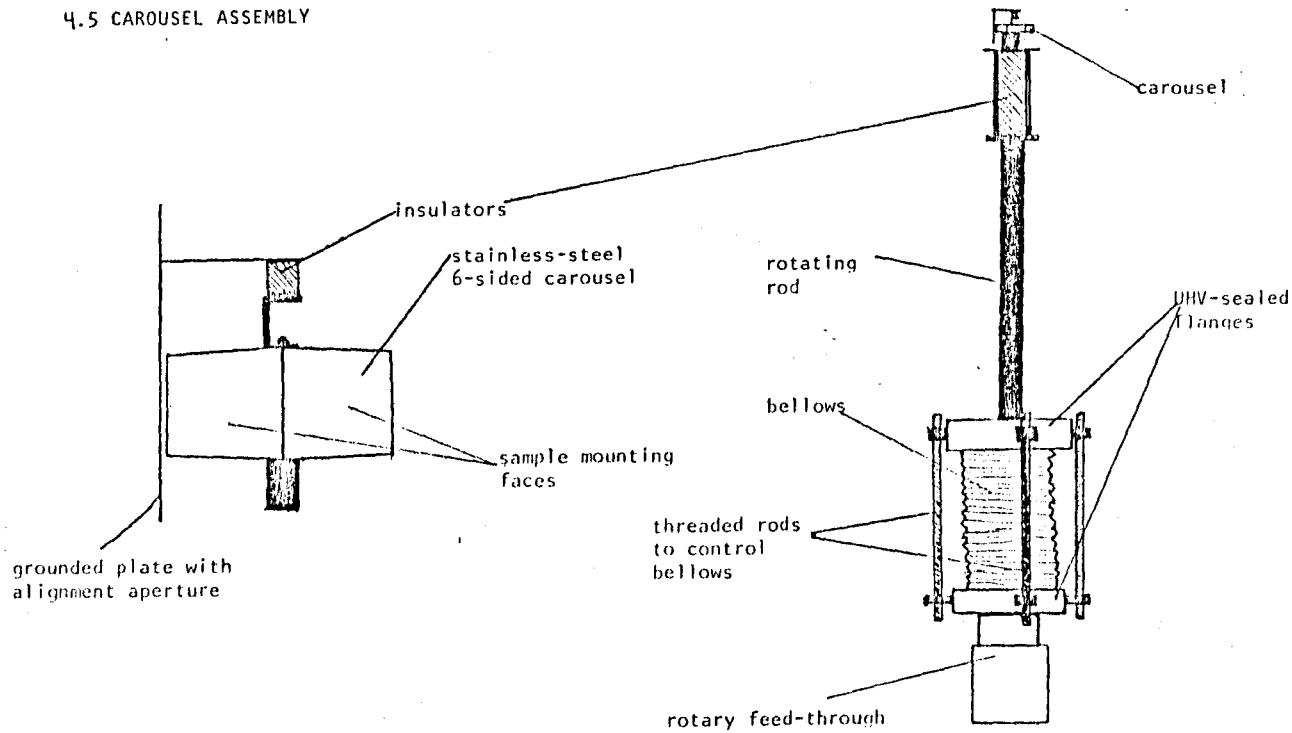

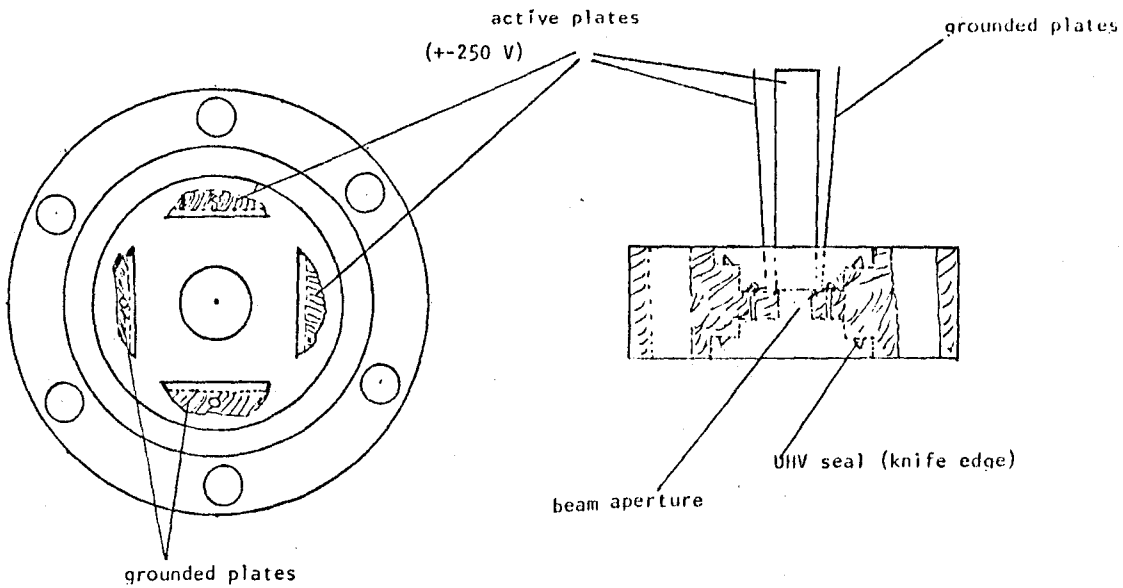

4.6 DEFLECTION PLATE ASSEMBLY (on two-sided flange)

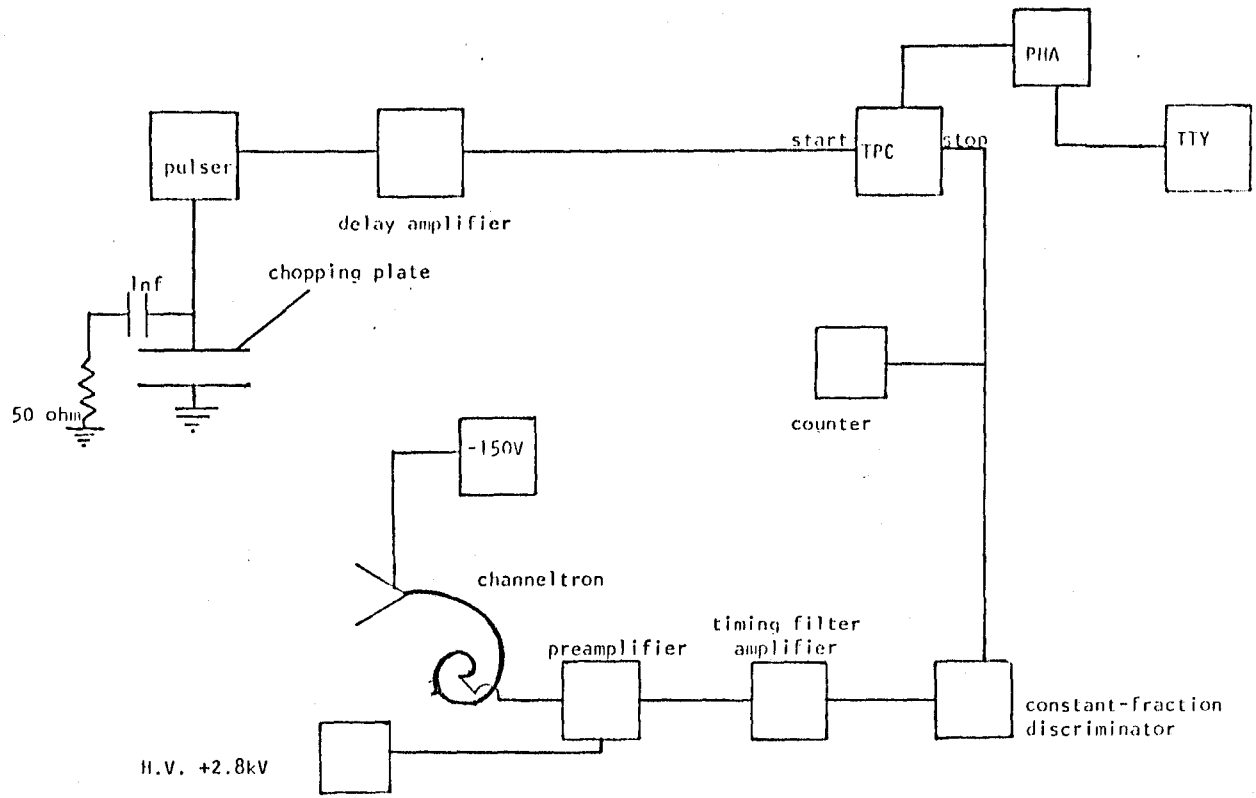

4.7 BLOCK DIAGRAM OF TOF ELECTRONICS

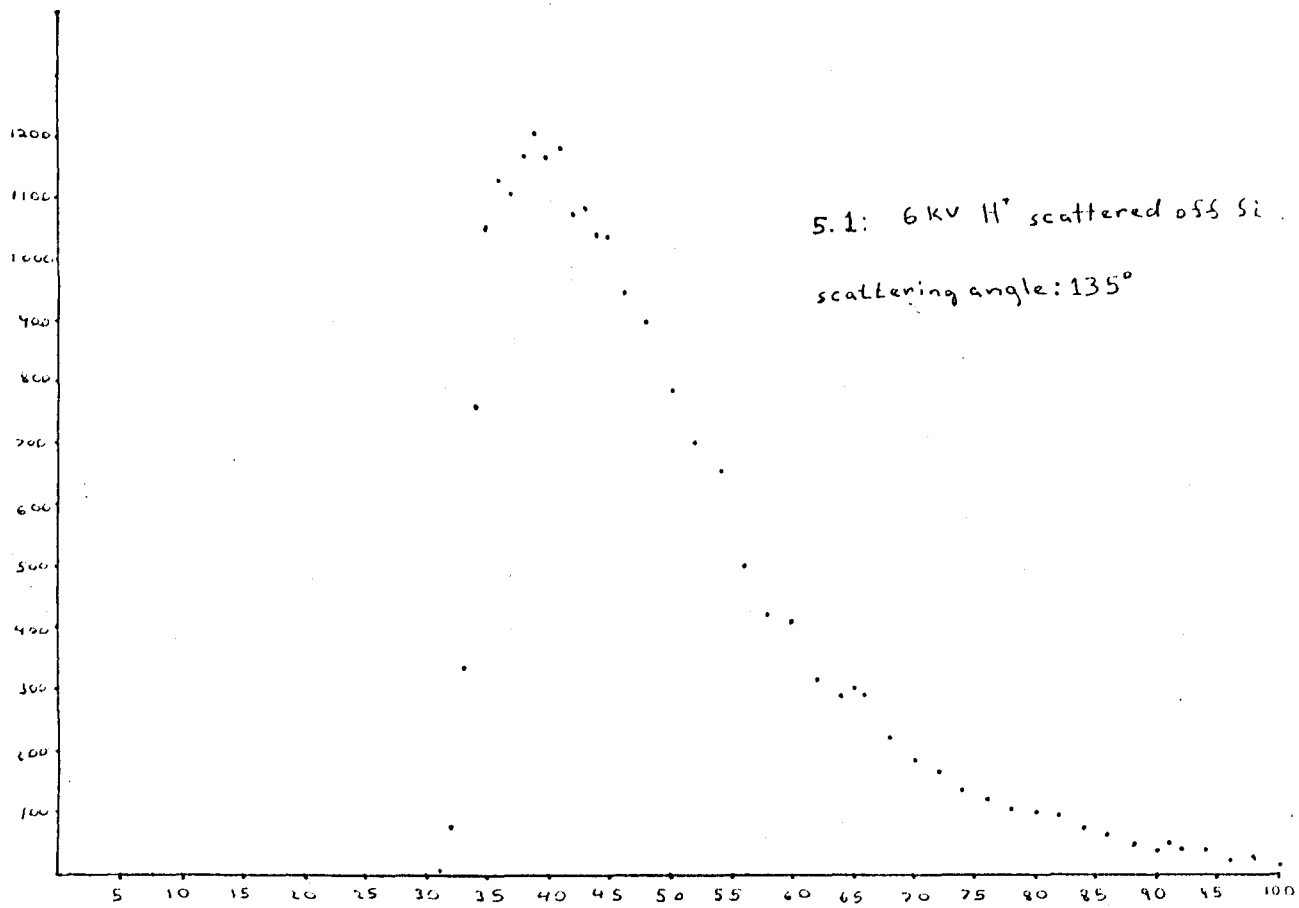

5.1: 6 KV H^+ scattered off Si

scattering angle: 135°

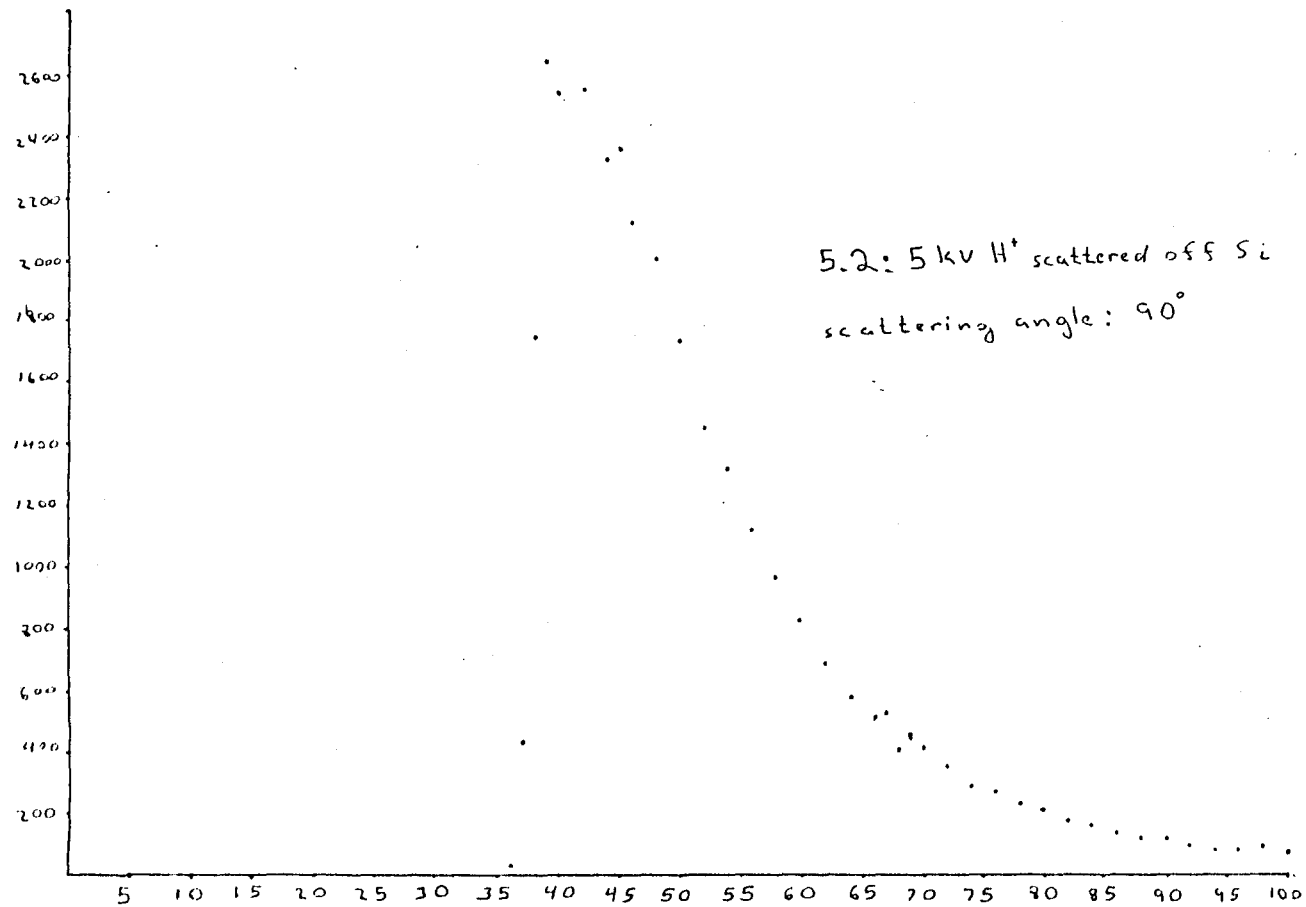

5.2: 5 kv H^+ scattered off Si

scattering angle: 90°

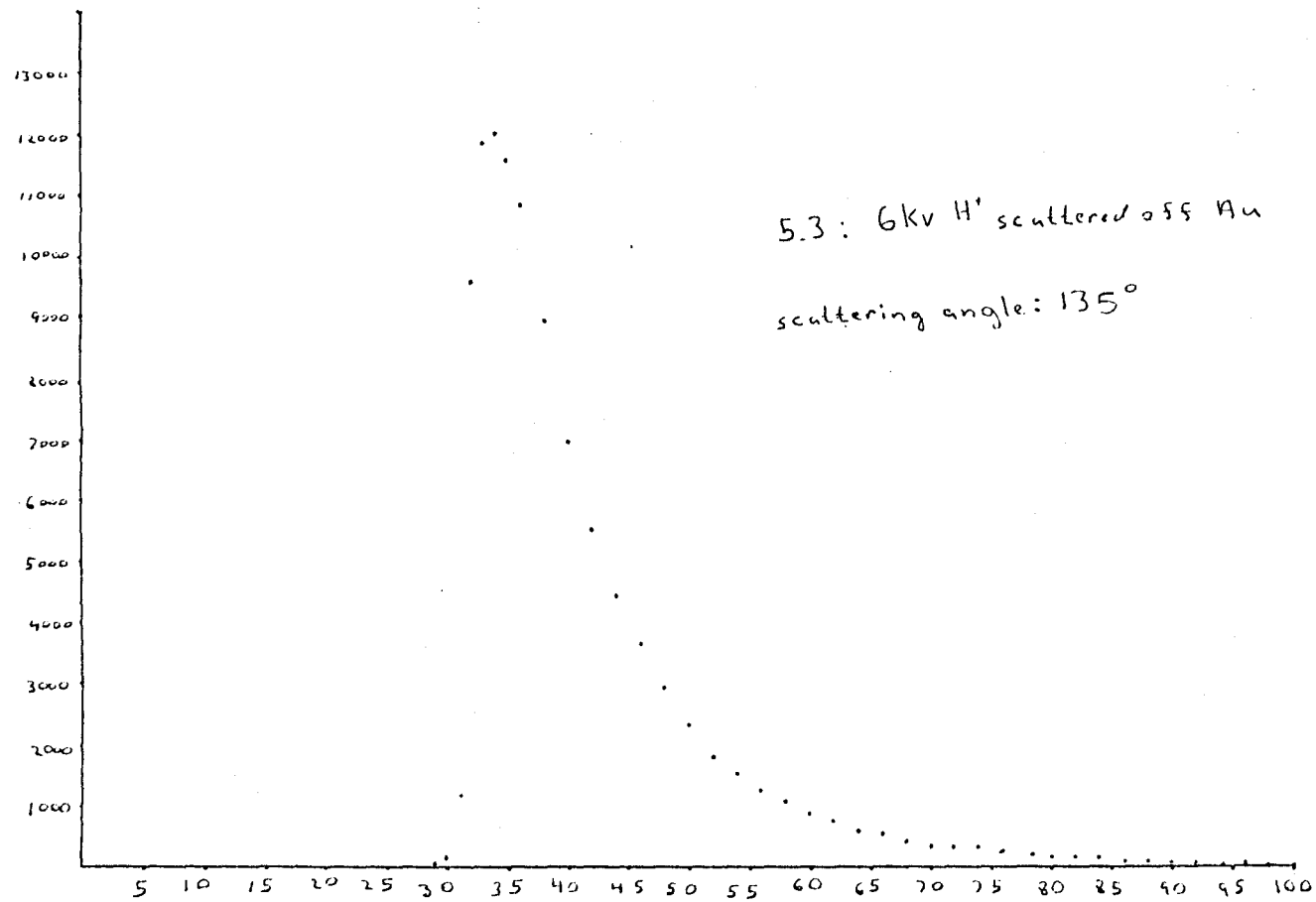

5.3: 6Kv H^+ scattered off Au

scattering angle: 135°

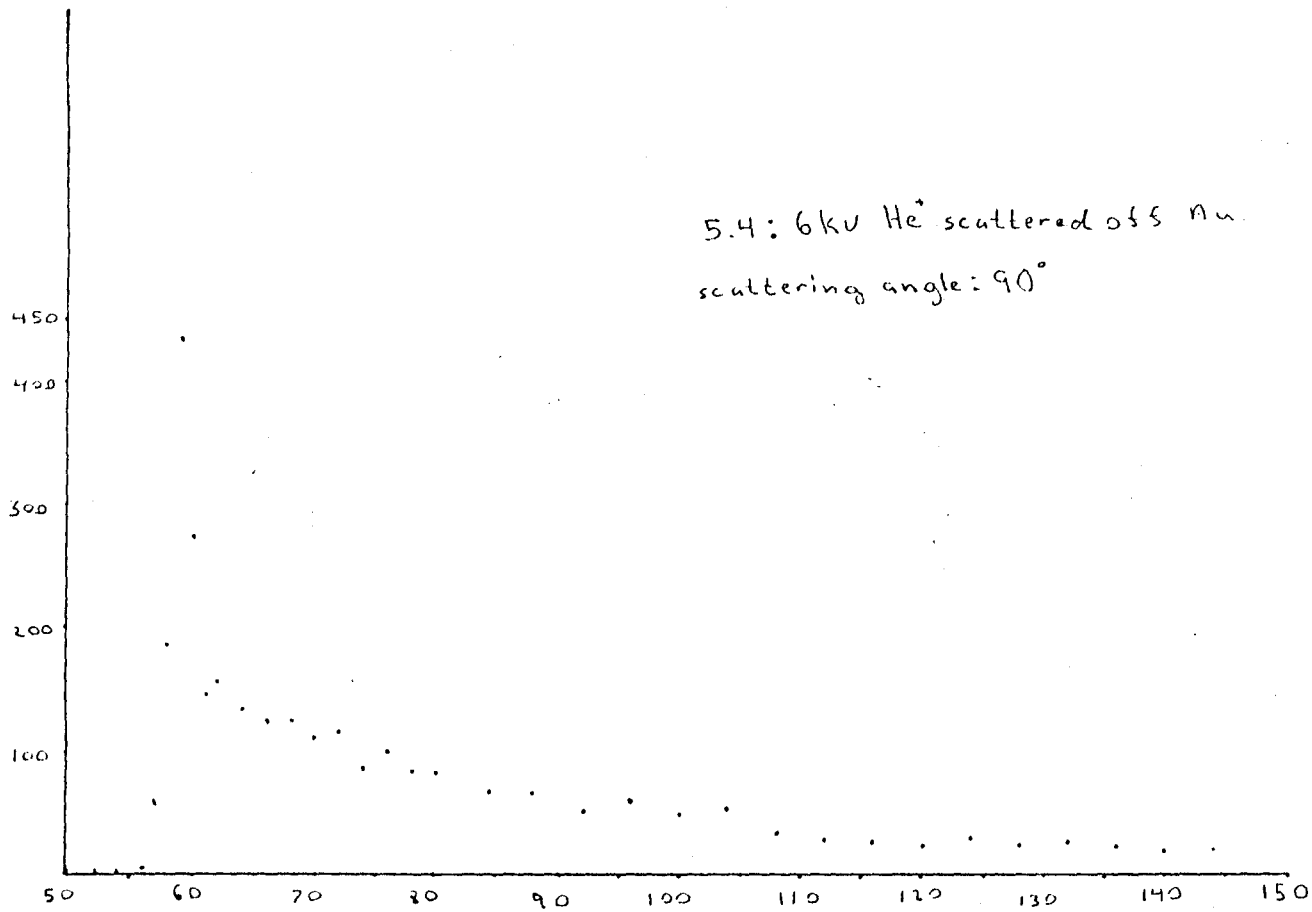
5.4: 6kV He+ scattered off Au
scattering angle: 90°
450
400
300
200
100
50
60
70
80
90
100
110
120
130
140
150

APPENDIX A

ION BEAMS AND LENSES

Theorem:

1) Any static electric field selects energy of charged particles, regardless of shape.
2) Any static magnet field, regardless of shape, selects the momentum of charged particles.

Proof:

1) Equations of motion of charged particles in an electric field;

$$\frac{m d^2\underline{r}}{dt^2} = q\,\underline{E}(\underline{r}) \qquad \text{let } S = \sqrt{\frac{\bar{q}}{m}}\,t, \text{ reduced time parameter}$$

$$\therefore \quad \frac{d^2\underline{r}}{dS^2} = \underline{E}(\underline{r})$$

This second order differential equation can be solved in principle given two initial conditions;

1. $\underline{r}_o$, the initial position, and
2. $d\underline{r}_o/ds = (E_o/q)^{1/2}\,\hat{u}$; $\hat{u}$ = direction of initial velocity, $|\hat{u}|=1$

$\therefore$ the path of the particle is completely determined by the initial energy and position.

2) Equations of motion of charged particles in a magnetic field;

$$\frac{m d^2\underline{r}}{dt^2} = \frac{q}{c} \frac{d\underline{r}}{dt} \times \underline{B}(\underline{r})$$

let:

$$s = \frac{q}{mc} t, \quad \therefore \quad \frac{d^2\underline{r}}{ds^2} = \frac{mc}{q} \frac{d\underline{r}}{ds} \times \underline{B}$$

$$= \frac{c}{q} \underline{p} \times \underline{B}$$

This equation can be solved, in principle, given;

1) $\underline{r}_o$, and

2) $d\underline{r}_o/ds = \underline{p}_o c/q$

$\therefore$ path is completely determined by the initial position and momentum.

Consider a cylindrical field, (as in an ESA):

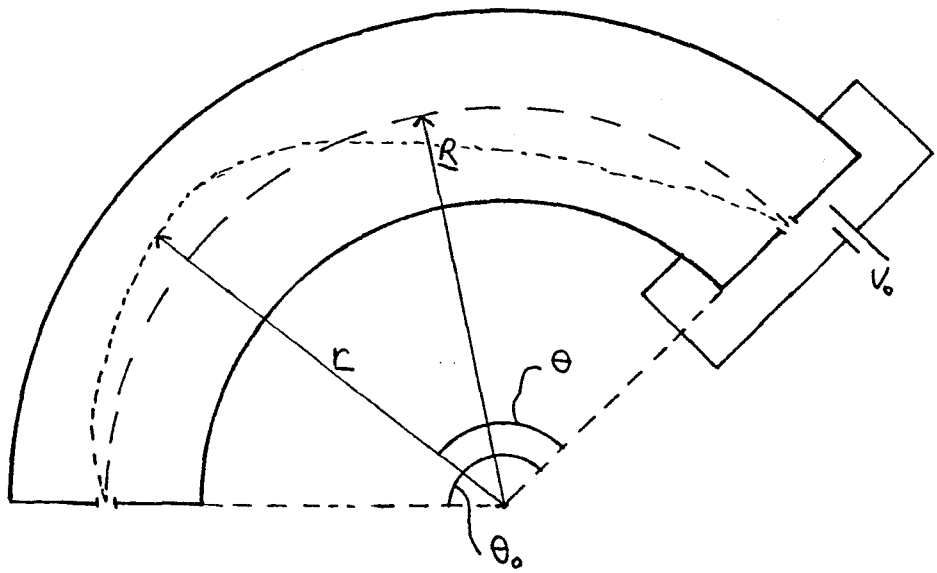

$\underline{R}$ defines equilibrium orbit

$\underline{r}$ defines the particle orbit

$$E_r(r) = E(R)\,(\frac{r}{R})^{-n} = \text{radial field}$$

for cylindrical fields n = 1:

$$E_r(r) = \frac{E_o R}{r},\quad E_o = E(R)$$

let $y = r-R$, expand $E_r(r)$;

$$E_r(r) = E(R+y) = E_r(R) + \frac{\partial E_r}{\partial r}\Big|_{\substack{y \\ r = R}} + \ldots\ldots$$

$$= E_o\,[1 + \frac{y}{R}]$$

Equations of motion;

$$\frac{md^2r}{dt^2} - r\,(\frac{d\theta}{dt})^2 = -qE_o\,(1 - \frac{y}{R})$$

On central path; $r = R$, $\frac{d\theta}{dt} = -\omega$, $(y = 0,\ \frac{d^2r}{dt^2} = 0)$,

$$-mR\omega^2 = qE_o \text{ and } m(\frac{d^2r}{dt^2}) - r(\frac{d\theta}{dt})^2 = -mR\omega^2\,[1 - \frac{y}{R}] \qquad (1)$$

Eliminate $\frac{d\theta}{dt}$;

$$m\,r^2\,\frac{d\theta}{dt} \backsim m\,R^2\omega$$

$\therefore$ $\frac{d\theta}{dt} = \frac{\omega R^2}{r^2}$, assuming small deviations from equilibrium orbit

$$\therefore \quad \left(\frac{d\theta}{dt}\right)^2 \simeq \frac{\omega^2 R^4}{r^4} \simeq \omega^2 \left(1 - \frac{4y}{R}\right)$$

substitute into Eq. (1):

$$\frac{d^2r}{dt^2} = -2\, y\omega^2 = \frac{d^2y}{dt^2}$$

$$\therefore \quad \frac{d^2y}{dt^2} + 2\,\omega^2 y = 0$$

$$\therefore \quad y = A\cos(\omega_{ot}) + B\sin(\omega_{ot})$$

$$\omega_o = \sqrt{2}\,\omega = \sqrt{\frac{2qE_o}{mR}}$$

$\therefore$ particles oscillate around the equilibrium orbit.

$\therefore$ if:

$$\omega_o t = \pi \text{ (for one full oscillation of y)}$$

$$\omega t = \frac{\pi}{\sqrt{2}} \equiv 127^\circ$$

$\therefore$ if; $y(0) = 0$, defined by slits then for $\omega t = 127^\circ$, $y = 0$.

$\therefore$ electrostatic analyzers are built as 127° (θ_o) cylindrical electric fields and collect output particles at the centre of the plates.

To calculate the energy that is analyzed:

let $x = \omega_o t$ (distance along path)

$\frac{1}{2} m\dot{x}^2$ = kinetic energy of ion = To = $\frac{1}{2} m\omega_o^2$

On central path: $m\omega_o^2 R = qE_o$

$\therefore$ $2T_o R = qE_o$

$\therefore$ particles of energy T_o will pass through the analyzer

$$T_o = \frac{qE_o}{2R}$$

Theorem:

Cylindrically-symmetric electric field regions between field-free regions act as converging lenses.

Proof:

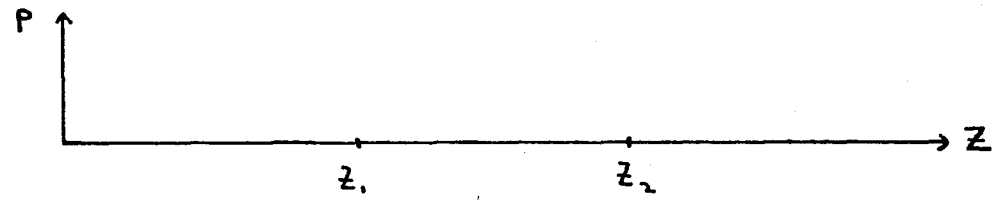

$\rho = 0$ defines axis of cylindrically symmetric field.

Z_1 to Z_2 is field region.

$\frac{d\rho}{dz} = \rho'$, defies angle of beam to z-axis.

Equation of motion[5]:

$$\rho'' + \frac{1}{2}\frac{v'}{v}\rho' + \frac{v''}{4v}\rho = 0 \qquad (2)$$

(ray equation for ion beams in cylindrically symmetric field).

v = axis potential, let

$$R = (-v)^{1/4}\rho, \quad (-v) > 0, \ \therefore\ (-v)^{1/4} > 0$$

Substituting in (2) gives:

$$R'' + \frac{3}{16}\left(\frac{v'}{v}\right)^2 R = 0$$

$$R'' = -\frac{3}{16}\left(\frac{v'}{v}\right)^2 R < 0, \text{ because } R > 0.$$

$\therefore$ $R'' < 0$ for all z between z_1 and z_2.

$\therefore \quad \frac{dR'}{dz} = -\frac{3}{16}\left(\frac{v'}{v}\right)^2 R$, integrate between Z_1 and Z_2

$\therefore \quad R_2' - R_1' = -\frac{3}{16} \int_{Z_1}^{Z_2} \left(\frac{v'}{v}\right)^2 R \, dZ$

$\therefore$ Since integral is +'ve

$$R_2' - R_1' < 0$$

$\therefore \quad R_2' < R_1'$

and

$$R_2' - R_1' = (-V_2)^{1/4} \rho_2' - (-V_1)^{1/4} \rho_1' \quad (\text{for } z < z_1 \text{ or } z > z_2,\ V' = 0)$$

$V_1 = V_2$, because field-free region outside $z_1 z_2$:

$\therefore \quad R_2' - R_1' = (-V_2)^{1/4} (\rho_2' - \rho_1') < 0$

now $V_2 < 0$ (define potential).

$\therefore \quad \rho_2' - \rho_1' < 0, \ \therefore \ \rho_1 < \rho_2$

$\therefore$ exit angle is smaller than entrance angle, this is converging lens.

Einzel Lens:

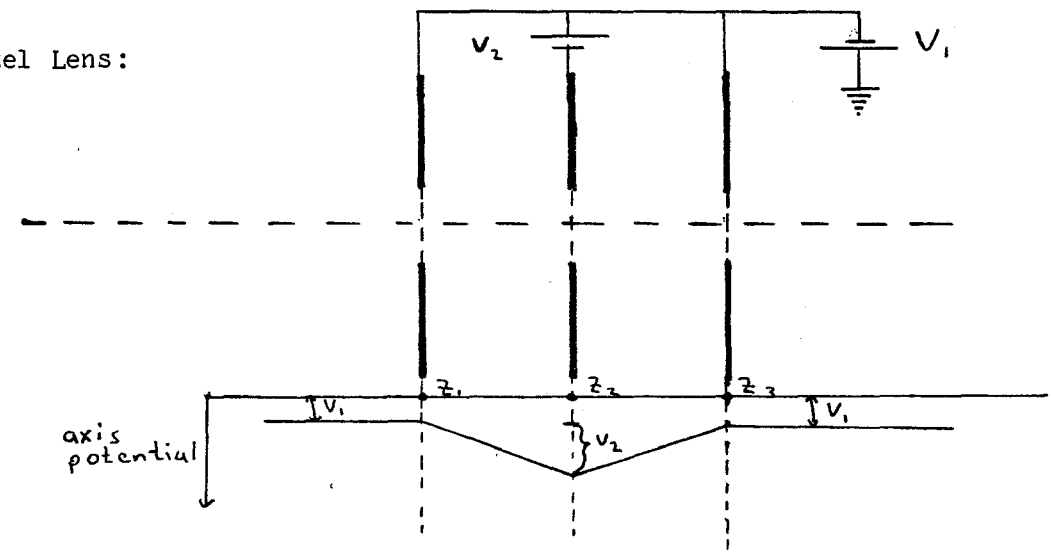

The lens is symmetric with:

$$\frac{1}{f_1} = \frac{1}{f_2} = \frac{-3}{8L}\left(\frac{V_2}{V_1} - 1\right)\left(3\sqrt{\frac{V_1}{V_2}} + \sqrt{\frac{V_2}{V_1}} - 4\right)$$

$$L = Z_3 - Z_2 = Z_2 - Z_1$$

APPENDIX B

VACUUM DEVICES AND CONCEPTS

A surface analyses using ion scattering must provide an environment for the surface that is free of contamination. Surfaces are contaminated by absorbing gases that strike the surface. To calculate the vacuum required the number of molecules striking the surface must be derived.[5] Consider velocity space:

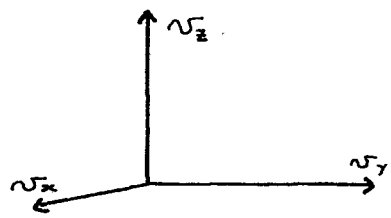

Arrange all velocity vectors at the origin. The spherical shell containing all vectors between v and v+dv has N_v vectors in it. Therefore, N_v = number of particles with velocity between v and v+dv. Area of the sphere = $4\pi v^2$.

In polar coordinates element of surface area on the shell is: $da = v^2 \sin\theta \, d\theta \, d\psi$, therefore the number of particles per unit volume with velocity between v and v+dv and directions between θ and $d\theta$ and ψ and $d\psi$ is:

$$d^3n = \frac{dn_v \, v^2 \sin\theta \; d\theta \, d\psi}{4\pi v^2} = \frac{dn_v \sin\theta \; d\theta \, d\psi}{4\pi}$$

where dn_v = density of particles in vacuum system with velocity between v and v + dv:

$$dn_v = \frac{Nv}{\text{volume of vacuum system}}$$

Consider area element dA in x-y plane projected on direction θ:

$$dA = \cos\theta d\theta$$

All particles within volume $v\cos\theta d\theta$ pass through dA in one second. Therefore, number of particles striking dA/second

$$= d^3n\ v\cos\theta d\theta$$

$$= \frac{vdn_v \cos\theta \sin\theta\, d\theta d\psi dA}{4\pi}$$

Therefore, number of particles striking unit area

$$= \frac{vdn_v \cos\theta \sin\theta\, d\theta d\psi}{4\pi}$$

Therefore, current density for particles with velocity between v and v+dv

$$= \int_0^{2\pi} \int_0^{\pi/2} \frac{(vdn_v \cos\theta \sin\theta\, d\theta d\psi)}{4\pi}$$

$$= \frac{vdn_v}{4}$$

Therefore, total current density

$$= .25 \int_0^{\infty} vdn_v = \frac{\frac{n}{4}\int_0^{\infty} vdn_v}{\int_0^{\infty} dn_v} = \frac{n\bar{v}}{4}$$

The choice of velocity distribution determines $\bar{v}$. If the distribution is Maxwellian:

$$\bar{v} = (8\ KT/\pi m)^{1/2}$$

Now the vacuum required to allow a reasonable time to perform the

analysis on the surface can be determined. The monolayer time is required.

Let:

D = density of particles in a monolayer

S_o = probability of particle sticking to surface

then

$$\frac{dn}{dt} = S_o J = \frac{S_o n \bar{v}}{4}$$

For monolayer:

$$\Delta t = \frac{4D}{S_o n \bar{v}} = \text{monolayer time}$$

eg.: for N_2; $D = 7 \times 10^{14}$ molecules/cm^2 and $\bar{v} = 5 \times 10^4$ cm/sec, assuming $S_o = 1$ have; (760 torr = 2.367×10^{19} molecules/cm^3) at 760 torr $\Delta t = 2 \times 10^{-9}$ sec, at 10^{-9} torr $\Delta t = 1600$ sec. Thus to allow time to do the experiment the target must be cleaned under ultra-high vacuum conditions and then analyzed.

If the target is heated S_o can be reduced to a very small number, increasing the monolayer time. This is why surface analysis systems operate below 10^{-9} torr, or have sample heating.

Reduction of S_o by heating is exploited to clean the walls of ultra-high vacuum systems. The system is baked at high temperature (100-150^{o}C) and all the absorbed gases in the walls are liberated and can be pumped out. Techniques such as this are essential for obtaining pressures below 10^{-8} torr.

Another important reason for ultra-high vacuum is to provide a long

mean free path for the ion beam so it will not disappear before it reaches the target. The mean free path is defined as the average distance between collisions. A simple derivation goes as follows: The cross-section for collision between two particles

= 2R for two identical particles

A particle sweeps out a cylinder of volume V_o, (radius 2R), in one second; $V_o = 4\pi R^2 (\bar{v})$. Number of particles in this cylinder

$= n4\pi R^2 \bar{v}$

= number of collisions/sec.

if we assume a Maxwellian distribution

Z = number of collisions/sec

$= \sqrt{2}\ 4\pi R^2 \bar{v}\ n$

T = time between collisions

$= Z^{-1}$ and

λ = mean free path

$$= T\bar{v} = \frac{1}{\sqrt{2}\ 4\pi R^2 n}$$

Thus λ is proportional to $(\text{pressure})^{-1}$. Therefore in long accelerators very low pressures must be used, 10^{-11} torr is not uncommon.

When the mean free path becomes longer than the dimensions of the vacuum chamber, collisions with the walls become more important than collisions with other particles, and thus dominate the transport phenomena. This condition is known as molecular flow.

When considering pumps and vacuum systems two concepts are used: pumping speed, defined as $S = \frac{dV}{dt}$, and throughput, defined as $Q = p\frac{dV}{dt} =$

the mass flow, through the pump or conductance. Pumping speed is most often quoted by the manufacturer of the pump but throughput is more useful. Units of throughput are (torr litre)/(sec). For example, time dependence of pressure in vessle of constant volume pumped at constant S[5]:

$$\frac{dpV_o}{dt} = -pS$$

$$V_o \frac{dp}{dt} = -pS$$

$$\therefore \quad \frac{dp}{p} = \frac{-S\ dt}{V_o}$$

$$\therefore \quad p_2 = p_1 \exp\left(-\frac{S}{V}(t_2 - t_1)\right)$$

Now the throughput of an aperture can be calculated:

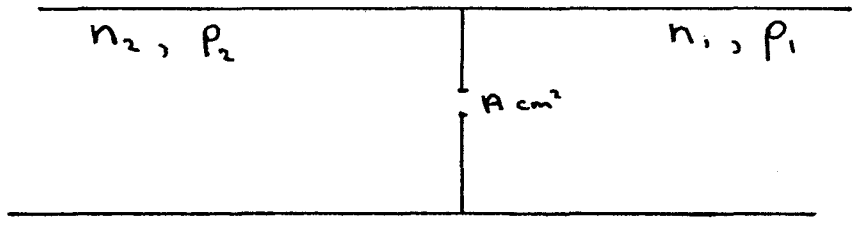

$$Q = p \frac{dv}{dt}$$

ideal gas law; pV = nRT. Gas is assumed ideal (molecular flow conditions), therefore for pressure p;

$$Q = p \frac{dV}{dt} = KT \frac{dn}{dt} = KTJ_p, \quad J_p = \text{particle current}$$

from 1st section; $J_p = nA\bar{v}/4$

$$Q_{21} = \frac{KT(n_2\bar{v}A)}{4} \quad \text{and} \quad Q_{12} = \frac{KT(n_1\bar{v}A)}{4}$$

Therefore,

$$Q_{net} = Q_{21} - Q_{12}$$

$$= \frac{KTA\bar{v}}{4}(n_2 - n_1)$$

$$= \frac{A\bar{v}}{4}(p_2 - p_1)$$

Now consider conductance defined as

$$Q = C(p_2 - p_1), \quad C = \text{conductance}$$

$\therefore$ for an aperture of area A,

$$C = \frac{A\bar{v}}{4}$$

The Knudson formula gives Q for a long conductance[5]:

$$Q = \frac{4/3\ \bar{v}\ (p_2 - p_1)}{\int_0^L \left(\frac{H(x)}{A^2(x)}\right) dx}$$

where

p_2 = input press

p_1 = output press

$H(x)$ = perimeter of conductance at x

$A(x)$ = cross-sectional area of conductance at x

For a long (L greater than R) tube;

$$Q = \frac{2\pi R^3 \bar{v}}{3L} (p_2 - p_1)$$

Therefore

$$C = \frac{2\pi R^3 \bar{v}}{3L}$$

For ideal aperture of radius R:

$$C = \frac{A\bar{v}}{4} = \frac{\pi R^3 \bar{v}}{4} = C_i$$

Therefore

$$C_{tube} = \frac{(8R)}{3L} C_i$$

A short tube gives:

$$\frac{8RC_i}{3L} \leq C \leq C_i$$

The Dushman formula gives C for all L[5]:

$$C = \frac{A\bar{v}}{4(1+3L/8R)}$$

Three main types of pumps were used on the system described here: roughing pump ($\geq 10^{-2}$ torr), high vacuum pump ($\geq 10^{-8}$ torr), and ultra-high vacuum pump ($\leq 10^{-8}$ torr).

The roughing pump was a rotary mechanical pump. The high vacuum pumps were on each section: the source section had an oil diffusion pump-cold trap combination, the differential section had an ion pump, and the UHV section had a turbomolecular drag pump. The UHV pumps were water-cooled Ti sublimation pumps, on the differential and UHV sections.

A brief description of each type of pump follows.

Rotary Mechanical Pump

The rotary pump works by taking a volume at intake pressure and compressing it to atmospheric pressure. The gas is released through a valve into the air. Lowest pressure for single-stage pumps is about 10^{-2} torr. Compression ratio (volume at intake press/volume at exhaust) is[5]:

$$\frac{V_{in}}{V_{out}} = \frac{nRT_{in}}{nRT_{out}} \frac{P_{out}}{P_{in}} = \frac{P_{out}}{P_{in}} = 8 \times 10^{4}$$

Sealing oil with low vapour pressure must be used to prevent leaks at the seals. A diagram of the pump appears below.

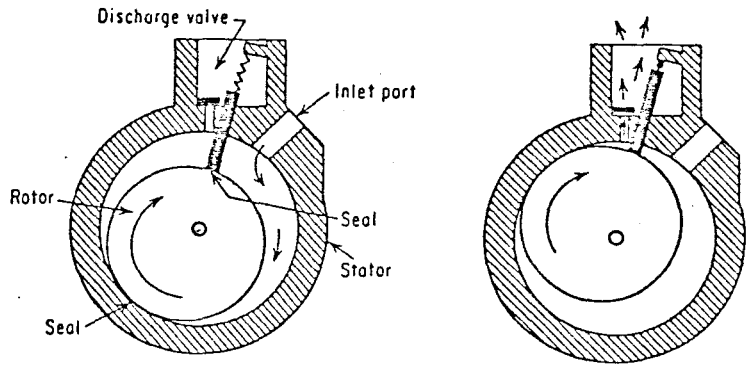

Oil Diffusion Pump

A working fluid (oil) is evapourated in a boiler and sent through nozzles in a downward stream. Gas molecules are caught in the jet and given a momentum downwards, causing a pressure difference. Oil

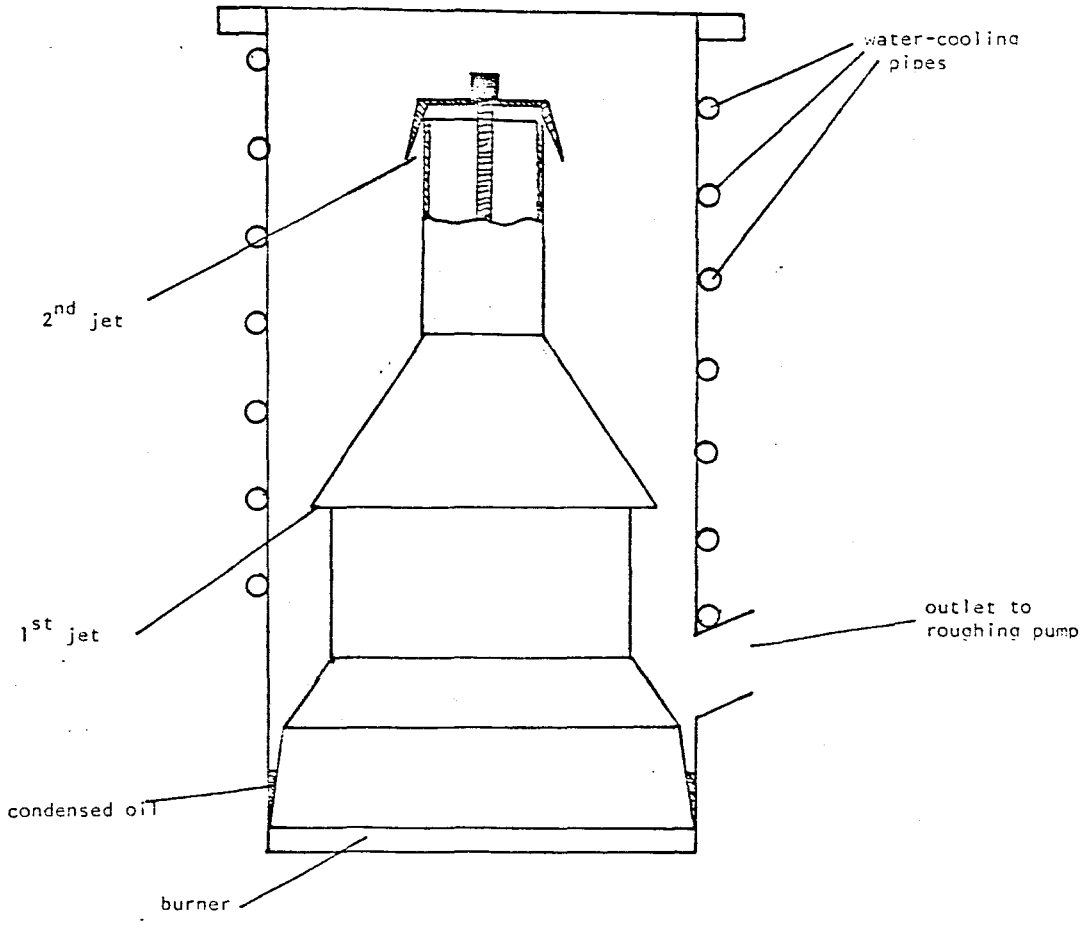

CUTAWAY VIEW OF OIL DIFFUSION PUMP

given a momentum downwards, causing a pressure difference. Oil condences in the walls (water-cooled) and flows down to the boiler. Usually two or three stages are used.

Four effects limit the vacuum that can be obtained:

1) The vapour pressure of the oil, best oils have v.p. of 10^{-10} torr.
2) Cracked oil compounds have a higher v.p. The effect of these compounds is reduced by fractionation; oil with cracked comp. flows down to boiler, the cracked comp. evaporate first and are sent to the lowest jet, the purest oil reaches the center of the boiler and is supplied to the highest jet.
3) Oil back-streaming; all pumps lose oil into the system. The amount is reduced by a cold cap over the highest jet and a liquid nitrogen trap between the pump and the system.
4) Gas molecules backscatter from the oil stream. This effect is small but cannot be reduced.

Compression ratio can be shown to be large by the following simple model:

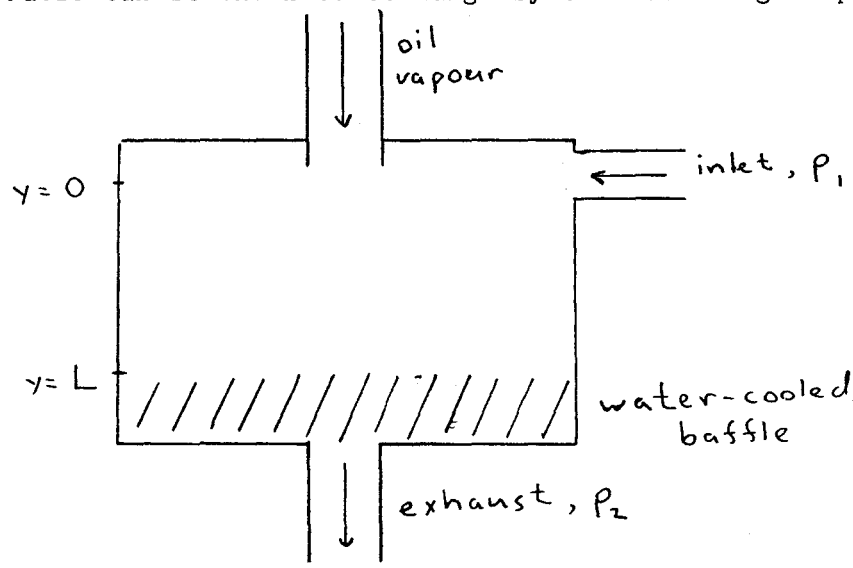

At $y = 0$, gas becomes entrained in oil vapour, aquiring downward velocity:

$$J_g = n_g u$$

The gas is compressed, therefore reverse flow is set up by diffusion:

$$J_r = \frac{dn_g}{dy} = \frac{1}{3} \lambda \bar{v} \frac{dn_g}{dy} = \frac{\bar{v}}{3\sqrt{2}\, \sigma n_v} \frac{dn_g}{dy} \quad , \lambda = \text{mean free path}$$

where; σ = cross-section for collision with oil molecule.

Therefore,

$$D = \frac{D_o}{n_v} \quad = \text{effective diffusion constant}$$

where n_v = density of oil vapour particles. At equilibrium, $J_r = J_g$, therefore:

$$\frac{Do}{n_v} \frac{dn_g}{dy} = n_g u$$

Therefore

$$\frac{p_2}{p_1} = \exp\left(\frac{u n_v L}{D_o}\right)$$

$\frac{u n_v L}{D_o} \sim 10^2$ for normal systems, $\therefore$ $\frac{p_2}{p_1} = e^{100}$, i.e. compression ratio is very large

A large range of pumping speeds are available, 50 litres/sec to 10^4 litres/sec.

Ti Sublimation Pump

This consists of a water-cooled baffle around a titanium-coated

tungsten filament within the vacuum system. Current is passed through the filament until a monolayer of Ti is evaporated onto the baffle surface. The Ti will absorb all gases striking it by physio- or chemi-sorption. Pumping speed is proportional to surface area; S = 10 litres/sec/cm^2. Lowest pressure (10^{-11} torr) is limited by the desorption of trapped gases.

Turbo-molecular Pump

This pump works on the principle of molecular drag. Under molecular flow conditions when particles collide with the wall they stick for approximately 1 msec, then are emitted isotropically, according to Lamberts law. The T-M pump has a rotor that revolves at high speed (20-50,000 rpm). The molecules that strike the rotor are given a drift velocity v_d. Molecules that strike the wall have their drift velocity reduced to 0.

Compression ratio can be calculated from the following model, where the rotor spins with its flat face against the stationary wall, into which are cut grooves to form a channel. In real pumps the height of the channel decreases as the pressure increases along it, to preserve molecular flow conditions, but we shall assume a constant depth of groove. A cross-section of one groove would appear as follows:

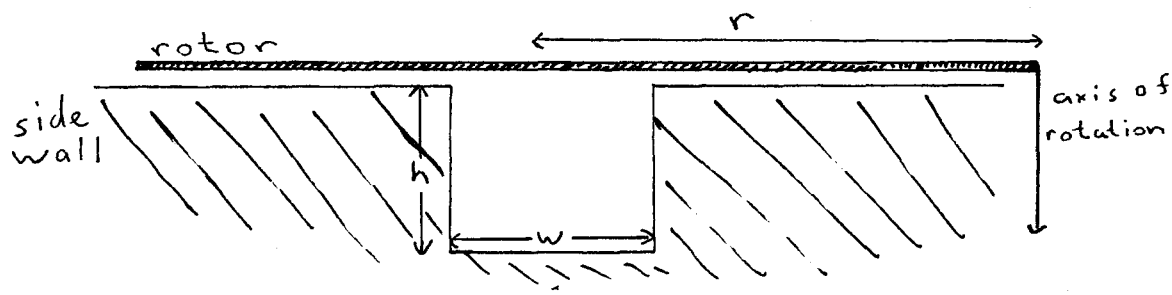

$$\text{drift velocity} = v_d = \left(\frac{\text{area of rotor exposed to channel}}{\text{total area of rotor and channel}}\right) v$$

$$= \frac{w\ v}{w+(w+2h)} = \frac{w\ v}{2(w+v)}$$

$$S = \frac{dv}{dt} = (\text{cross-section of groove})\ v_d$$

$$= \frac{h\ w^2\ v}{2(w+h)}$$

$$Q = PS = \frac{h\ w^2\ vP}{2(w+h)}$$

As the pressure difference increases a counter-flow is established according to Knudson's formula:

$$Q = \frac{4/3\ \bar{v}(p_2-p_1)}{\int_0^L H/A^2\ dx}$$

for short L (= dx)

$$Q = \frac{4\ \bar{v}\ A^2\ dp}{3\ H\ dx}$$

$$= \frac{4\ h^2\ w^2\ \bar{v}}{6(w+h)}\ \frac{dp}{dx}$$

where $A = hw$ and $H = 2(w+h)$. Maximum pressure difference when $Q_{back} = Q_{pump}$ or:

$$\frac{dp}{dx} = \frac{3pv}{4h\bar{v}} \quad \text{or} \quad \frac{p_2}{p_1} = \exp\ \frac{3L}{4h}\left(\frac{v}{\bar{v}}\right) = (\text{for average pump})\ e^{16.5} \sim 10^7$$

Thus, the compression ratio is large.

Turbo refers to the design of the pump used in this system; the

rotor was driven by a compressed air turbine and ran on air bearings, producing a completely oil-free vacuum. The pumping speed was 150 litres/sec at 47,000 rpm.

Ion Pump

The ion pump, sometimes known as the ion getter pump, ionizes the gas molecules and accelerates them to a cathode made of a getter, usually Ti. Electrons are used to ionize the gas. Their path length is increased by applying a magnet field so they spiral, producing a long path. A diagram of one section appears below. The ion pump used in the system had six of these sections. Ion pumps work from .01 to 10^{-11} torr.

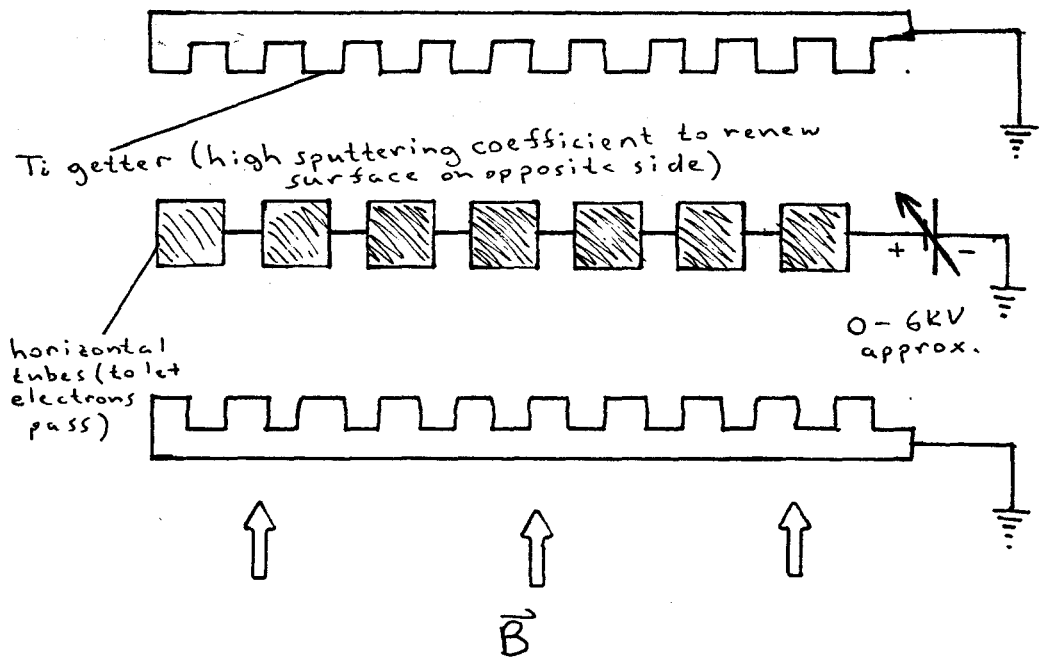

APPENDIX C

THE DUOPLASMATRON ION SOURCE

The original duoplasmatron ion source was designed in 1959 by Manfred von Ardenne. At that time conventional RF ion sources were reaching the limits of their current capability. Current was usually increased by scaling the smaller sources. This meant that a large plasma had to be maintained and focused. Large gas flows were needed to maintain the plasma and very large potentials wer needed to focus the beam to a reasonable size. These high potentials separated the charges and space-charge effects became important requiring large fields to hold the plasma together. The potentials required began to exceed the breakdown voltage of a polished electrode in the vacuum that could be maintained in the source section.

The duoplasmatron overcame these problems. The basic discharge was redesigned into a three-electrode discharge between a filament and the exit aperture. An intermediate electrode confined the discharge into a small region near the exit aperture. The second improvement was a magnetic mirror to focus the discharge into a small point at the exit aperture. The ion density at the exit aperture is thus about 10^4 times the ion density of the RF source at the exit aperture.

Ions are not extracted by fields, they are allowed to drift through the aperture and then are accelerated. The discharge as a whole remains neutral and no space-charge effects are encountered. Exit apertures of

10^{-2} in. radius are used allowing high vacuum to be obtained on the other side of the aperture. High vacuum allows high potentials to be used to accelerate the ions without breakdown.

A cross-section of the source used in this project is shown in figure C-1. The wiring diagram is shown in figure C-2. The source came with an Einzel lens to extract and focus the beam. It is included in the wiring diagram but not in the cross-section of the source.

The power supply was built in-house. The source required the following voltages and currents:

1) 0 to +10 kv variable, for the accelerating potential.

2) 0 to -3 kv variable, for the focus voltage.

3) 5 v at 30 amps, for the filament.

4) 150 v at .25 amps, initial and 75 v at 2 amps, running; for the arc (variable current).

5) 5 v at 1 amp, for the magnet, variable current

6) 0 to -500 v variable, for the extraction electrode (see text); 2,3,4 and 5 float at the accelerating voltage so an isolation transformer had to be used to supply power. The circuit diagram of the final power supply is shown in Figure C-3.

The arc supply proved to be the most difficult to design. Initially a SCR was used as a switch to initiate the arc but the transients eventially blew it out. A high current transistor solved this problem and gave a very stable, controllable arc current.

The extraction electrode supply was initially a simple voltage doubler giving 0 to -500 V. Arcing problems and discharge between the

extraction electrode and source occurred with this supply and it had to be abandoned. Since the source was designed to be run at 30 kV extraction operation below 10 kV led to ion buildup in the region of the exit aperture because of insufficient field gradient. To alleviate the problem a high negative potential was used on the extraction electrode, about -4 kV. This gave good stability.

The low extraction voltage gave other problems as well. The magnet could not be used at all. Increasing the current to the magnet reduced the current considerably. Possibly space-charge effects in the region of the exit aperture were to blame for this.

As can be seen from the wiring diagram the lens voltage floats on the accelerating voltage. The focus is between two negative potentials forming a very strong lens. Reducing the potential on the focus electrode with the focus control on the power supply reduced the current drastically. The reason for this is the configuration of the system. The first aperture into the mass-analyzing section is less than 20 cm from the end of the Einzel lens. To focus the beam onto the aperture required a very strong lens.

Since the source gave acceptable performance without the magnet and focus controls these were not thought to be serious disadvantages. The only way to obtain more current on target would be to focus the beam on the faraday cup aperture.

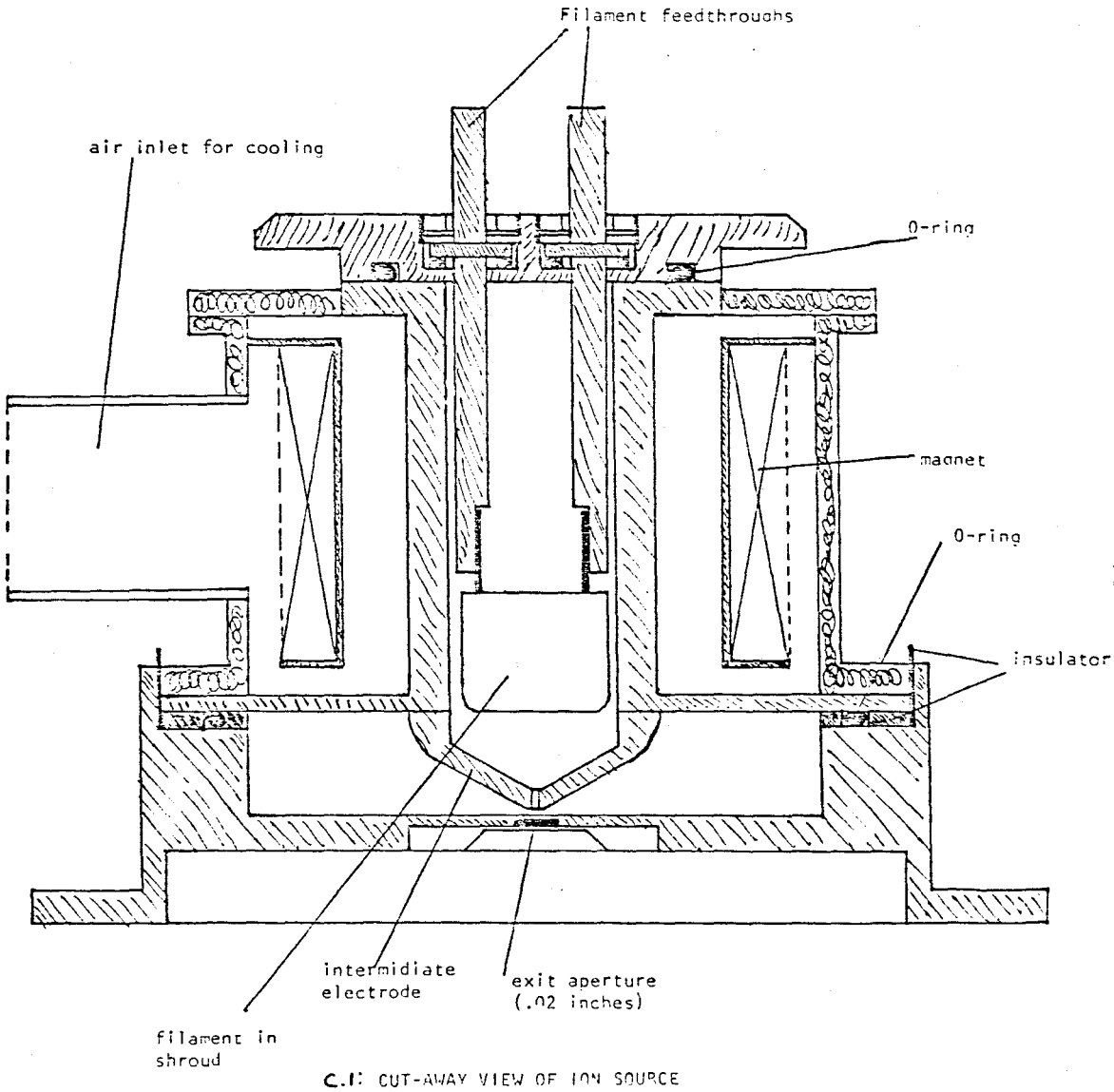

C.1: CUT-AWAY VIEW OF ION SOURCE

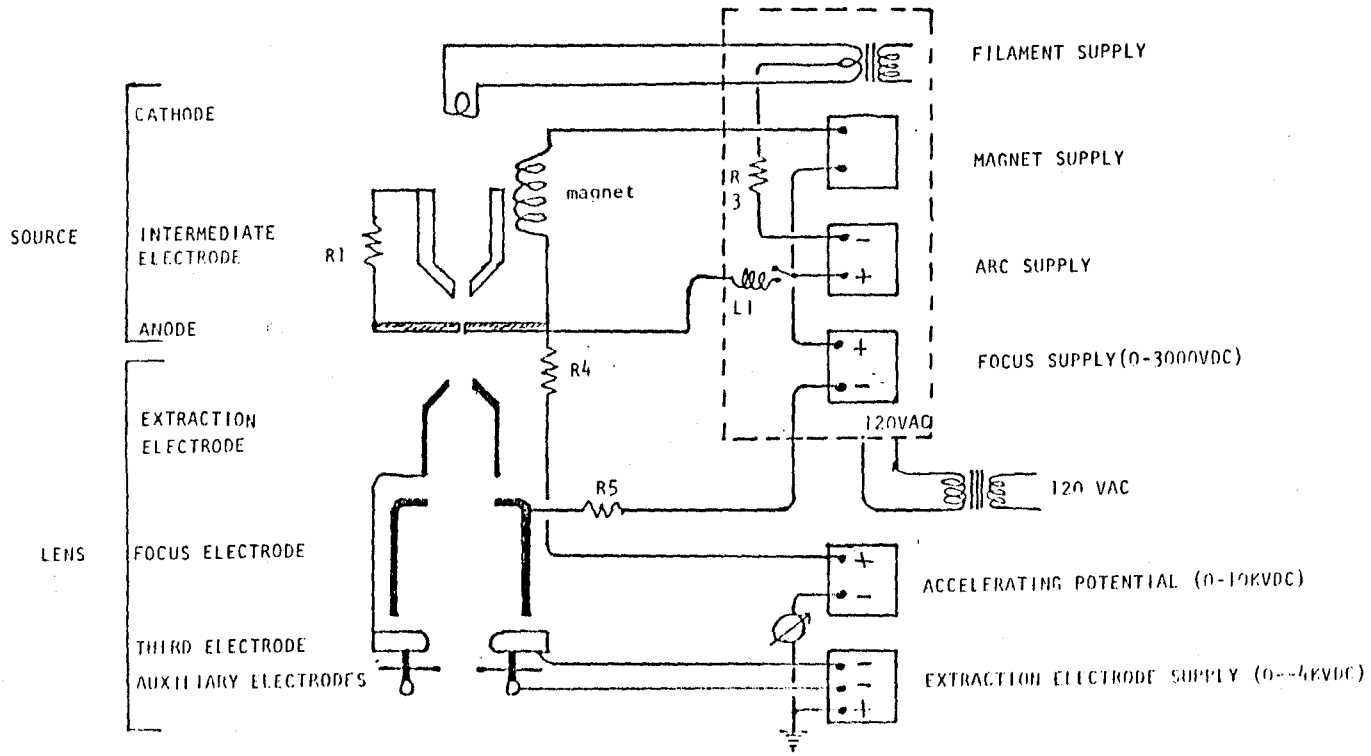

C.2: SOURCE INTERCONNECTIONS AND SUPPLIES

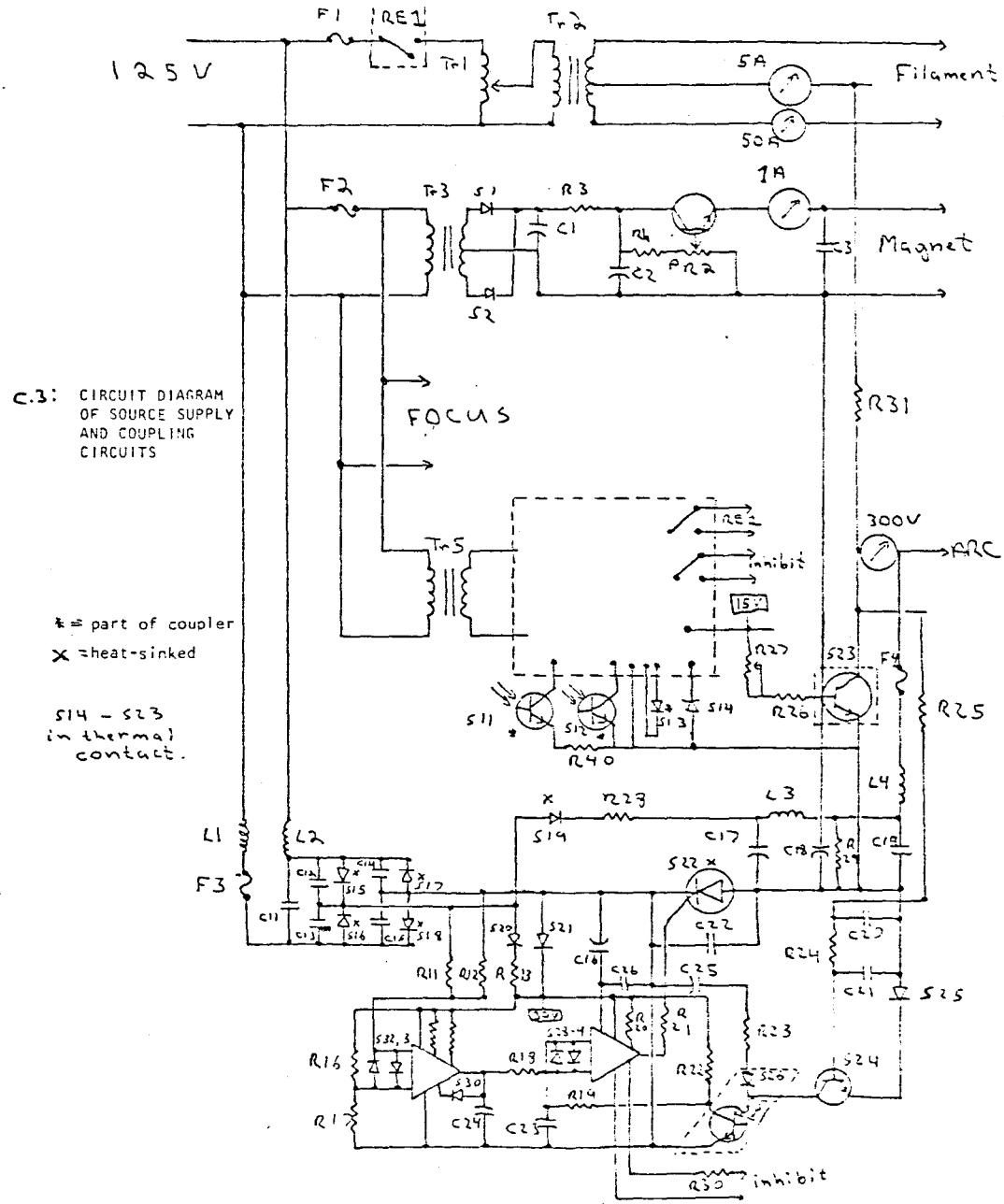

C.3: CIRCUIT DIAGRAM OF SOURCE SUPPLY AND COUPLING CIRCUITS

* = part of coupler

X = heat-sinked

S14 – S23 in thermal contact.

REFERENCES

1. Investigation of Low-energy Ion Scattering as a Surface-Analysis Technique: Surface Science, 30 (1972), 69-90, Ball et al.

2. Energy and Mass Spectra of Neutral and Charged Particles Scattered from Gold Surfaces: Y.S. Chen et al., Surface Science, 62 (1977), 133-147.

3. Comparison of TOF and ESA in Low-energy Ion Scattering: Buck et al., Nuclear Instruments and Method, 149 (1978), 591-594.

4. Backscattering of 5-15 KeV Light ions from Silicon, Ph.D. Thesis, S.A. Agamy, McMaster University.

5. Private communication, Dr. A. van Weingaarden, University of Windsor, Dept. of Physics.

6. Duoplasmatron Ion Source for use in Accelerators: C.D. Moak et al., Rev. Sci. Inst., Vol. 30, number 8, August 1959, 694-699.